Spatiotemporal development of coexisting wave domains of Rho activity in the cell cortex

Siarhei Hladyshau
School of Biology, Georgia Institute of Technology, Atlanta, GA
Mary Kho
School of Biology, Georgia Institute of Technology, Atlanta, GA
Shuyi Nie
School of Biology, Georgia Institute of Technology, Atlanta, GA
Denis Tsygankov (denis.tsygankov@bme.gatech.edu)
Wallace H. Coulter Department of Biomedical Engineering, Georgia Institute of Technology and Emory University, Atlanta, GA

Research Article

Keywords: Rho family GTPases, wave domains, spatiotemporal regulation, cell-level actin dynamics

Posted Date: March 17th, 2021

DOI: https://doi.org/10.21203/rs.3.rs-300938/v1

Version of Record: A version of this preprint was published at Scientific Reports on September 30th, 2021.
See the published version at https://doi.org/10.1038/s41598-021-99029-x.

Spatiotemporal development of coexisting wave domains of Rho activity in the cell cortex

Siarhei Hladyshau[1], Mary Kho[1], Shuyi Nie[1], Denis Tsygankov[2]*

[1]School of Biology, Georgia Institute of Technology, Atlanta, GA.
[2]Wallace H. Coulter Department of Biomedical Engineering, Georgia Institute of Technology and Emory University, Atlanta, GA.

*To whom correspondence should be addressed

The Rho family GTPases are molecular switches that regulate cytoskeletal dynamics and cell movement through a complex spatiotemporal organization of their activity. In *Patiria miniata* (starfish) oocytes, such activity generates multiple co-existing regions of coherent propagation of actin waves. Here we use computational modeling to investigate the development and properties of such wave domains. The model reveals that the formation of wave domains requires a balance of the autocatalytic activation and the negative feedback in the Rho signaling motif. Intriguingly, the development of the wave domains is preceded by a stage of low-activity quasi-static patterns, which may not be readily observed in experiments. Spatiotemporal patterns of this stage and the different paths of their destabilization define the behavior of the system in the later high-activity (observable) stage. Accounting for a strong intrinsic noise allowed us to reproduce wave dynamics in both *Patiria miniata* and *Xenopus laevis* (frog). For quantitative comparison of simulated and experimental results, we developed an automated method of wave domain detection, which revealed a sharp reversal of pattern formation in the middle of anaphase in starfish oocytes. Overall, our findings provide an insight into spatiotemporal regulation of complex and diverse but still computationally reproducible cell-level actin dynamics.

1. Introduction

Rho family small GTPases are the key regulators of cytoskeletal organization and dynamics [1, 2] and have been a subject of an extensive research effort in the biomedical community. Advanced optogenetic approaches revealed a complex, coordinated spatiotemporal dynamics of Rho activity during cell motion [3-5]. Although GTPases and their regulators GEFs (guanine nucleotide exchange factors) and GAPs (GTPase-activating proteins) are a part of a large and complex signaling network [6], the emerging cell-level activity of GTPases exhibits characteristic patterns of wave propagation or static formations that have been studied mathematically in many other biological contexts [7-14]. Recently, a particular type of mathematical models, mass-conserved activator-substrate models (MCAS), also referred to as wave-pinning models [15-18], have gained popularity because they account for the switch-like behavior of GTPases due to their autocatalytic activity [19] and successfully capture polarization patterns observed in experiments [17, 18, 20-22]. These models include autocatalytic (positive) feedback that amplifies small perturbations and allows cell to generate a strong, persistent response to a weak local cue. Coupling of such autocatalytic activation with a local inhibition (negative feedback) generates diverse dynamic regimes depending on the parameters representing the strength of the feedbacks [23]. For example, Holmes *et al*. [24] have shown that even a one dimensional model (1D) with three components, including active and inactive forms of a nucleation-promoting factor and the inhibition through F-actin, can generate a stable polarization patch, oscillating polarization patch, reflecting waves, a single terminating wave, wave train, and more exotic formations.

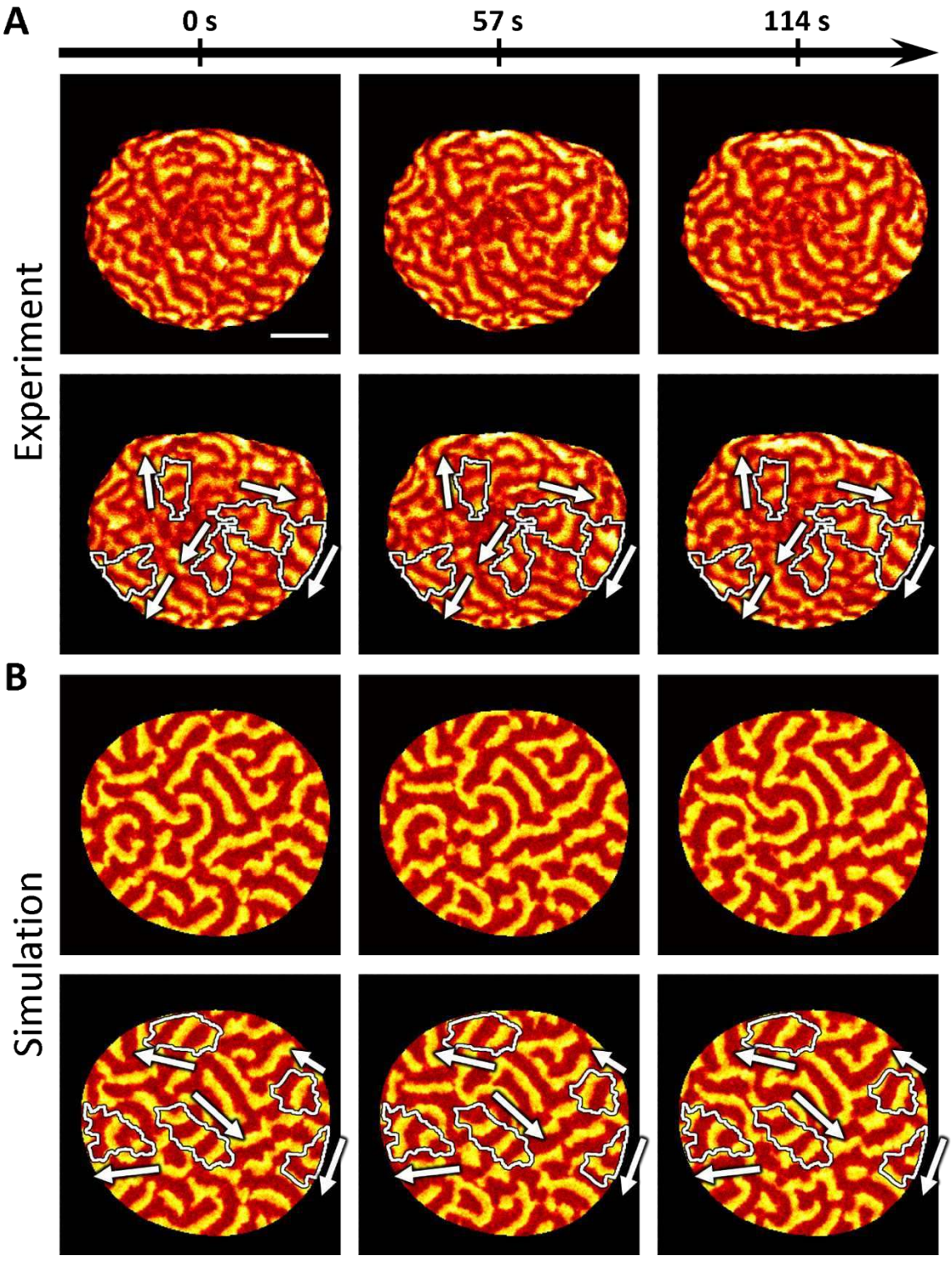

Figure 1. Cortical waves of Rho activity in *Patiria miniata* oocytes during anaphase before the formation of cytokinetic furrow. Both the experiment [25] and our model show similar overall dynamics and the presence of wave domains. **A.** Snapshots of wave propagation in the experiment [25]. The scale bar is 50 μm. **B.** Snapshots of wave propagation in our simulation ($k_0 = 0.2$, $s_2 = 1, \alpha_{1,2} = 2$). The white contours outline wave domains as defined in the following section, while the arrows indicate the direction of wave propagation in these domains. For the full dynamics see Supplemental Video 16 in [25] and Supplemental Video 1.

In this work, we use a two-dimensional version of the MCAS model coupled with local inhibition to investigate a particular type of wave dynamics that, to our best knowledge, was not studied in the biological context, but was recently observed in *Patiria miniata* (starfish) oocytes [25]. Shortly after the initiation of anaphase, starfish oocytes generate cortical waves of the active form of Rho-GTPase, followed by the front of F-actin polymerization. An interesting aspect of such dynamics is partitioning of the whole cell area into seemingly independent regions of wave propagation, henceforth referred to as *wave domains* (**Fig. 1A**). Each domain is characterized by coherent wave propagation with a small variance of the direction of wave-vector. In the neighboring domains, waves propagate in different (often the opposite) directions with respect to each other. Such dynamics is very different from the formation and competition of multiple spiral waves, which is often observed in excitable media [10, 13, 14]. Indeed, spiral waves have wave-vectors that point in all directions away from the spiral center. Our simulations show a strikingly close resemblance of the model behavior and the experimental time-lapse records (**Fig. 1B** and **Supplemental Video 1**). Visually, the dynamics is very complex because the domains do not remain static but gradually change their shape and number over time. However, our analysis reveals the underlying processes that drive the initiation and development of the wave domains.

One of the challenges in the analysis of the spatiotemporal behavior in a biological system is that an experimental observation may correspond to a transient behavior of the model. For example, in our model, one of the competing wave domains eventually wins, taking all the available space. This happens on a time scale much larger than the cell cycle, so that mitosis in experiments occurs well before we could see the final stages of the simulated dynamics. This is a problem because formal mathematical analysis of dynamical systems typically relies on identifying steady states and performing the stability analysis in their vicinity [26, 27]. Thus, to study the details and the scope of possible transient behaviors (far from a steady state), we have to rely on a systematic analysis of the parameter space using simulations.

In this work, we first characterize the parameter regimes responsible for different types of dynamic behavior. We show that oscillatory behavior and instability of the homogeneous steady state is not enough for the formation of wave domains and additional restrictions on the activation rate and the strength of negative feedback are required. Next, we show that the observed dynamic regimes are preceded by the development of distinct low-intensity patterns at an earlier stage of the formation process. Finally, we show that the way the system transitions from low-intensity patterns to high-intensity dynamics defines the resulting types of spatiotemporal Rho activity.

Furthermore, we explored the effects of strong intrinsic noise in the system and showed that in addition to starfish dynamics, our simulations also *quantitatively* agree with our data on F-actin dynamics in *Xenopus laevis* (frog) embryos. However, this dynamic behavior is drastically different from the starfish oocytes. Our analysis showed that frog dynamics corresponds to a different regime in parameter space when wave domains cannot be developed.

An important part of this work is a methodology that we developed for automated identification of wave domains in time-lapsed image records. We used this method for quantitative characterization of wave domains and for comparison of our simulation with an experimental example of Rho activity in starfish oocytes. Our analysis revealed a time point during anaphase when Rho dynamics *abruptly* changes on the cell level. At this moment, the process of wave domain development reverses to a gradual breakup ending with the loss of wave propagation before mitosis.

3. Results

3.1 Overview of the model behaviors and the definition of wave domains.

Some of the dynamics regimes of our two-dimensional model (**Fig. 2A** and Methods) are analogous to the one-dimensional version studied by Holmes *et al.* [24]. However, the increase of dimensionality can also lead to the emergence of novel dynamic behaviors (**Supplemental Figure S1** and **Supplemental Video 2**).

In 1D model with a weak negative feedback, initial local spike of activity develops into a polarized state, which is a characteristic property of the MCAS systems. In the presence of strong inhibition, the model shows rich dynamics [23, 24]. In the so-called *excitable regime*, the system returns to the spatially homogeneous state if the initial local stimulus is weak. With a strong enough local stimulus, the model generates single terminating or reflecting traveling waves. Alternatively, in the *oscillatory regime*, in the presence of limit cycle and the unstable homogeneous state [24], small perturbations are sufficient to generate wave trains or more exotic patterns. In the 2D case, the formation of a near-boundary patch naturally corresponds to the polarized state in 1D. However, in the excitable and oscillatory regimes, the 2D model generates spiral waves, which cannot be observed in the 1D setup, but is a well-characterized feature of excitable systems previously studied with other models [28-30].

Intriguingly, in addition to the well-known spiral waves, in a particular region of parameter space of the 2D model, the system generates a more complex dynamics behavior (**Fig. 1A, B**), which closely resembles dynamics of the active form of Rho GTPase and F-actin in the cortex of starfish oocytes [25]. In this parameter regime, the system self-organizes from the homogeneous unstable state into multiple coexisting regions with persistent directions of the wave propagation that are different among the regions. We refer to these formations as *wave domains* and define them as sub-regions of the cell area with

(1) low variance of the wave vector direction,
(2) size larger than the wavelength of the activity waves propagating inside, and
(3) time scale of their boundary movement larger than the time scale of the wave propagation.

Figure 2B provides an example of such dynamics. Similar to spiral waves, the fronts of high concentration of the activator *A* (green channel in **Fig. 2C**) are followed by the refractory regions with an increased concentration of the inhibitor *F* (red channel in **Fig. 2C**). However, visual representation of the directions of the wave vector (**Fig 2D**) clearly shows domains of unidirectional propagation, which is different from the surrounding areas. Typically, the shapes of the wave domains are elongated in the direction of the wave propagation inside it. The domains can be outlined along the regions of steep gradient of the direction of wave vectors (**Fig 2E**). Previously, regions with high-variance of wave directions (phase-defects) were reported by La Porta *et al* [31] for ethanol-water mixtures in the presence of temperature gradient. Also, regions of locally coherent waves were observed *in vitro* in the bacterial Min system [32], although the overall system behavior is different from the actin waves in starfish oocytes.

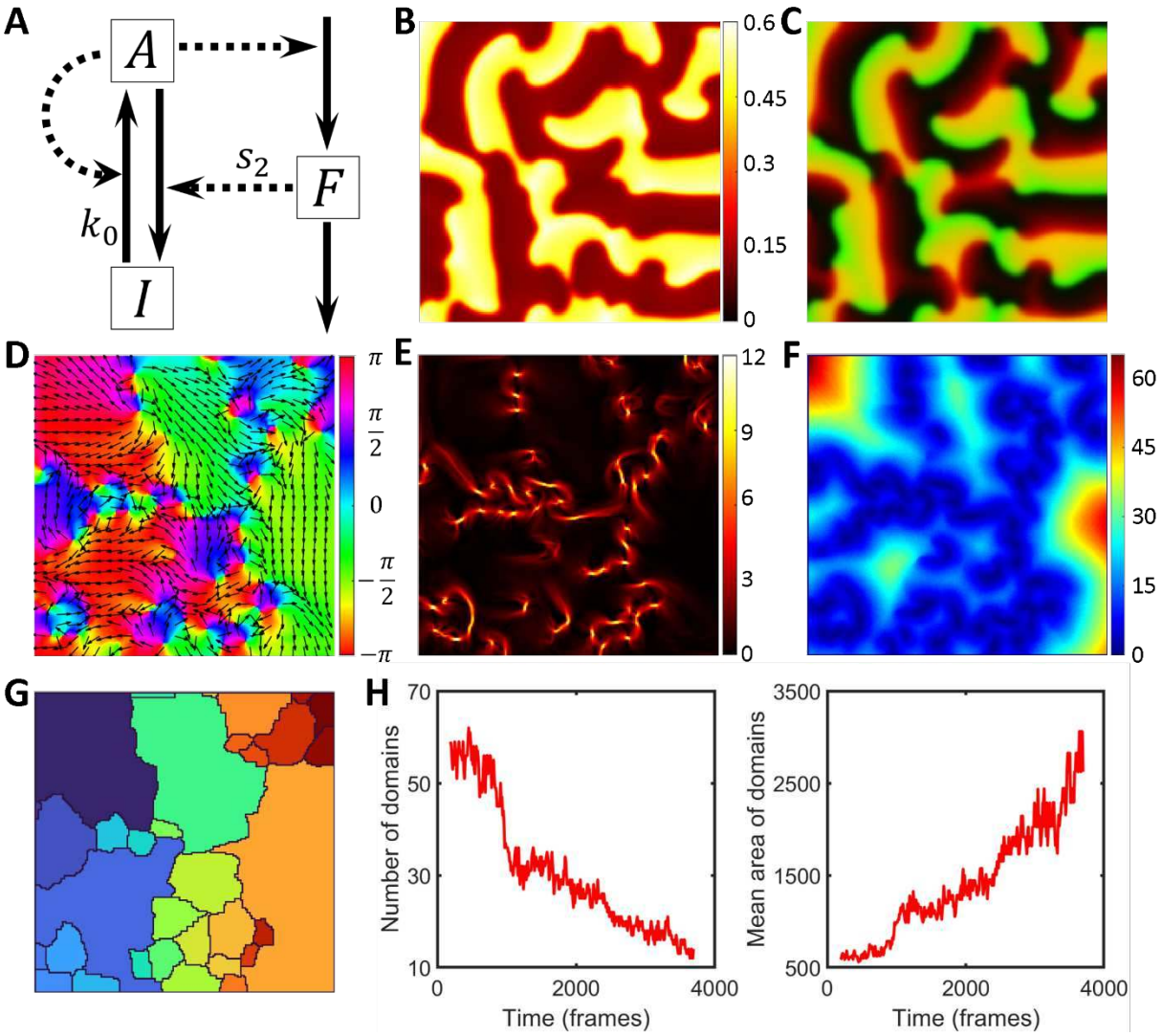

Figure 2. The model and an illustration of the wave domain concept. A. Diagram of the signaling motif. A and I represent active and inactive forms of the signaling molecule, while F represents a local inhibitor. **B.** The resulting distribution of component A in a snapshot of the simulation with $k_0 = 0.15$, $s_2 = 0.8$ using homogeneous initial conditions. **C**. An image of two merged channels: green channel represents activator A and red channel represents inhibitor F. The concentrations were scaled as $[C - min\ (C)]/[max(C) - mi\,n(C)]$. **D**. The colormap of the direction angles, θ, of the wave vectors at the same time frame as B and C. Arrows represent the direction of wave vectors. **E**. The colormap of the magnitude of a local change (gradient) in the directions of the wave vectors. Regions of high gradient are located at the edges of wave domain. **F**. The colormap of our metric of the coherence distance. **G**. Segmentation of the coherence distance with the modified watershed algorithm and after merging domains with similar values of the mean θ. **H.** The dynamics of wave domains. The number of regions detected by the automated segmentation pipeline is decreasing (left panel), while the mean area of regions is increasing over time (right panel).

3.2 Automated identification of wave domains in time-lapse images.

To investigate the properties of wave domains and their formation process in an unbiased way, we developed a method for automatic identification of the regions of coherent wave propagation. We used the time averaged values of the directions of wave vectors (see Methods) to suppress the regions with minor temporal fluctuations and to highlight the regions where wave propagation is persistent over a significant period of time. The shapes of such regions change over a longer time than the oscillation period of the activator dynamics. Based on the wave vector angles, θ, we define a metric of the coherence distance for each pixel as the maximal radius of the circle, within which the circular standard deviation [33] is smaller than a predefined critical value ($C_{cr} = 0.4$, **Fig. 2F**). Next, the metric is processed with our customized watershed algorithm. This algorithm is different from the MATLAB's watershed [34] in that flat regions of the input image are automatically merged with the regions that grow during the watershed process. This modification reduces over-segmentation. The result is further post-processed to merge the regions with the difference of mean θ values smaller than 0.5 radians and the length of their interface larger than 10% of the square root of the domain area (**Fig. 2G)** (see **Supplemental Figure S2**).

This method allowed us to perform the quantitative analysis of wave domains by computing their number and size as functions of time. In case when the initial homogeneous state is unstable, the system starts forming a large number of small regions, which gradually decreased in number and increase in size, thus generating wave domains over the course of the simulation. (**Fig. 2H**).

3.3. A balance of the basal activation rate and the negative feedback defines a distinct wave domain regime of the parameter space.

Next, we investigated how the formation of wave domains is regulated by the basal Rho activity (parameter k_0) and the strength of negative feedback from F-actin (parameter s_2). **Figure 3A** shows the parameter-space scan, with the snapshots of the spatiotemporal patterns in the oscillatory regime, while the excitable regime remains inactive for the homogeneous initial conditions with the minimal noise, $\alpha_{1,2} = 10^{-15}$ (see **Supplemental Video 3**). The increased inhibition is associated with the increase in the size of the refractory region (**Fig. 3A**) and the decrease of the total level of Rho activity (**Fig. 3B**). Both increasing and decreasing inhibition (the left and right sides of the oscillatory regime) lead to the formation of large spirals and a decrease in the image entropy (**Fig. 3C**, **Supplemental Video 3**, and **Methods**). The entropy is highest in the middle region of the parameter space, where we see the formation of wave domains. Finally, in the lower-left region, where both activation and inhibition are low, waves have large activation fronts, which prevents the formation of wave domains and leads to patterns with a high image correlation (**Fig. 3D**).

Thus, wave domains are formed only for a subset of parameter values, corresponding to the oscillatory regime of the system where the proper balance between the basal rate of activation and the strength of negative feedback is maintained.

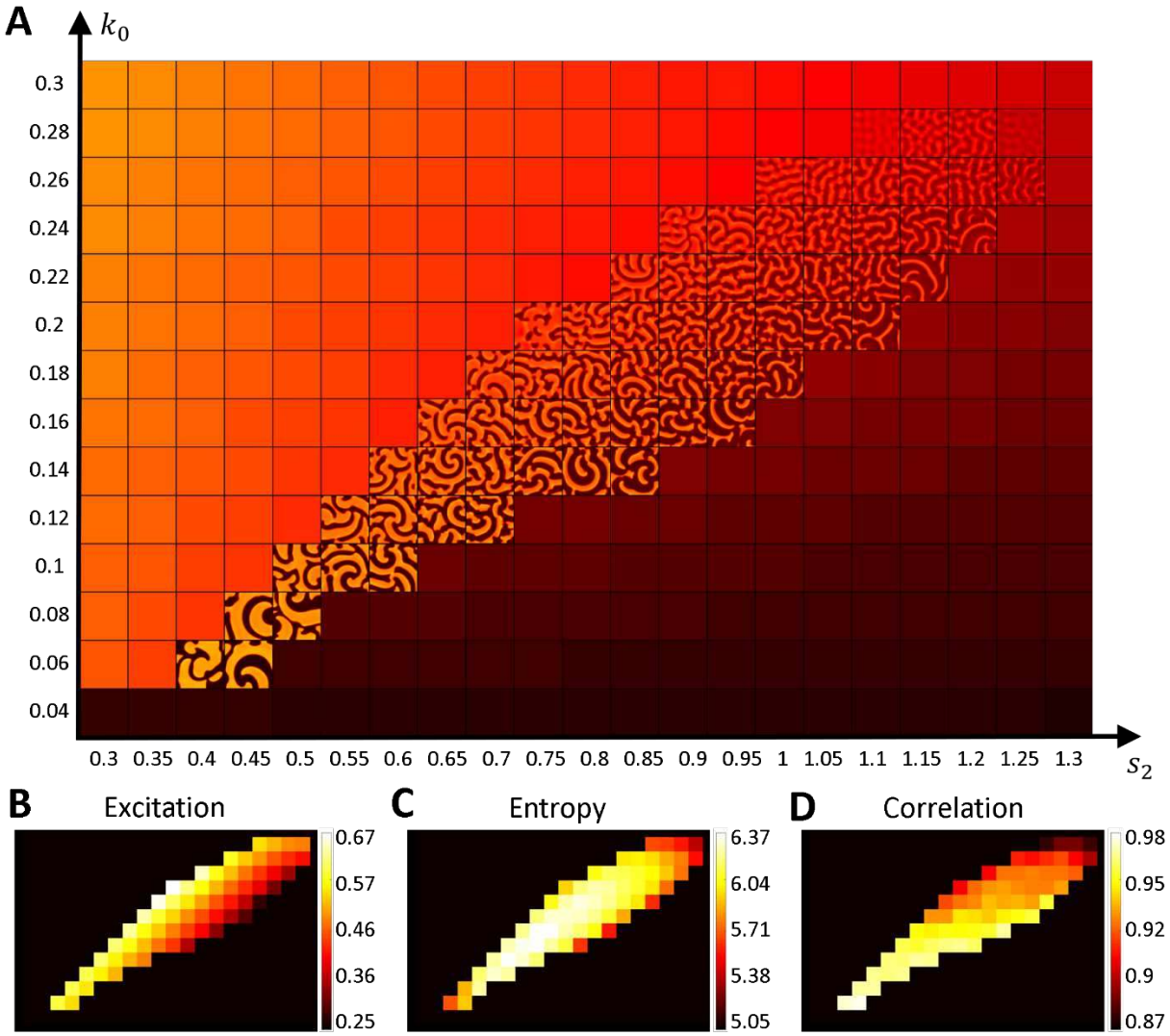

Figure 3. Parameter scan and textural analysis of the emerging patterns. A. The result of model simulations for a range of parameters k_0 and s_2 (see also Supplemental Video 3). **B**. The colormap of the excitation measure (see Methods) for the parameter space in A. **C, D**. The textural measures of pattern entropy and correlation for the parameter space in A. Each measure was averaged over 100 simulation steps after the formation of waves from the initial homogeneous state.

3.4. The spontaneous formation of wave domains proceeds in two distinct stages of dynamic behavior.

To better understand the process of wave domain formation, we looked closer at how the system behavior changes over time (**Figure 4A, B**). In our simulations, small perturbations in the homogeneous state start to grow persistently (low-activity stage) until the difference between the maximal and minimal concentrations of the activator reaches and stays at a nearly constant level (high-activity stage). The distinction between the stages becomes clearly visible when the activity level is plotted in log scale (**Fig. 4C, D**).

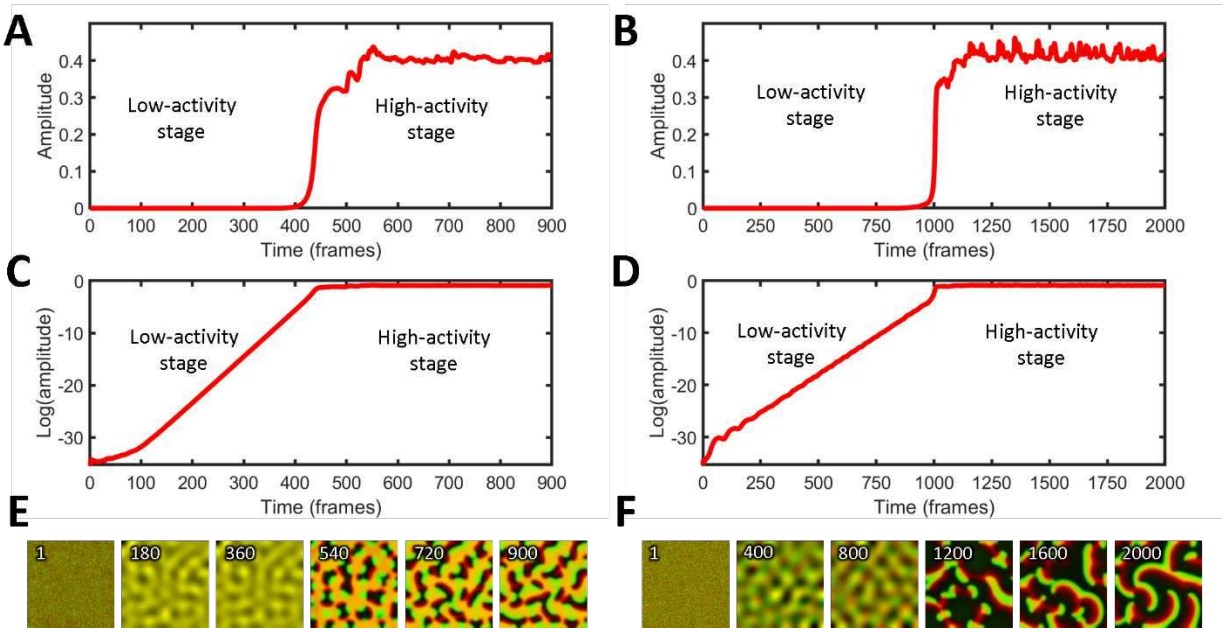

Figure 4. Two stages of pattern development. A, B. The concentration of activator A during the low- and high-activity stages for the quasi-static low-activity regime ($k_0 = 0.2$, $s_2 = 0.8$) and the oscillatory low-activity regime ($k_0 = 0.2$, $s_2 = 1.1$), respectively. **C, D.** The same plots as in A, B, but in the log scale. **E, F.** A series of snapshots of the system behavior from the same parameters as in (A, C) and (B, D), respectively (see also Supplemental Videos 4-6). The concentrations were scaled as $[C - min\ (C)]/[max(C) - min(C)]$ for both the inhibitor (red channel) and the activator (green channel) before the channels were merged together.

Although the activity in the earlier stage grows exponentially with time, its spatial distribution has a specific pattern with a well-defined periodic structure (see time frames 180 and 360 in **Fig. 4E** and time frames 400 and 800 in **Fig. 4F**). In order to see the activity at this low level, the images are scaled individually between the min and max concentration values of the current frame. Depending on parameters, such patterns in the low-activity stage can be quasi-static (**Fig. 5A**) or oscillatory (**Fig. 5B**). However, the shape of activity peaks and the period of oscillations do not change until the system enters the high-activity stage. The quasi-static low-activity stage develops at intermediate values of the negative feedback (white region in **Fig. 5C** and the central part of the parameter space in **Fig. 3C**), when the pattern entropy is high. In this regime, both activator and inhibitor are co-localized and have identical spatial distributions (**Supplemental Video 4, 5**). In contrast, the oscillatory low-activity stage is associated with high or low negative feedback and high values of k_0 (red regions in **Fig. 5C** and the low entropy part of the oscillatory regime in **Fig. 3C**). In this regime, the activator and inhibitor periodically switch spatial peaks moving out of phase (**Supplemental Video 6**). The quasi-static and oscillatory regimes are also associated with different durations of the low-activity stage. The duration is small when the strength of negative feedback (parameter s_2) has intermediate values but rapidly increases at higher and lower values of s_2 (**Fig. 5D**). In contrast to the low-activity stage, the high-activity stage is always dynamic. The inhibitor and activator concentrations do not overlap in space, and the time delay between their peaks drives the wave propagation.

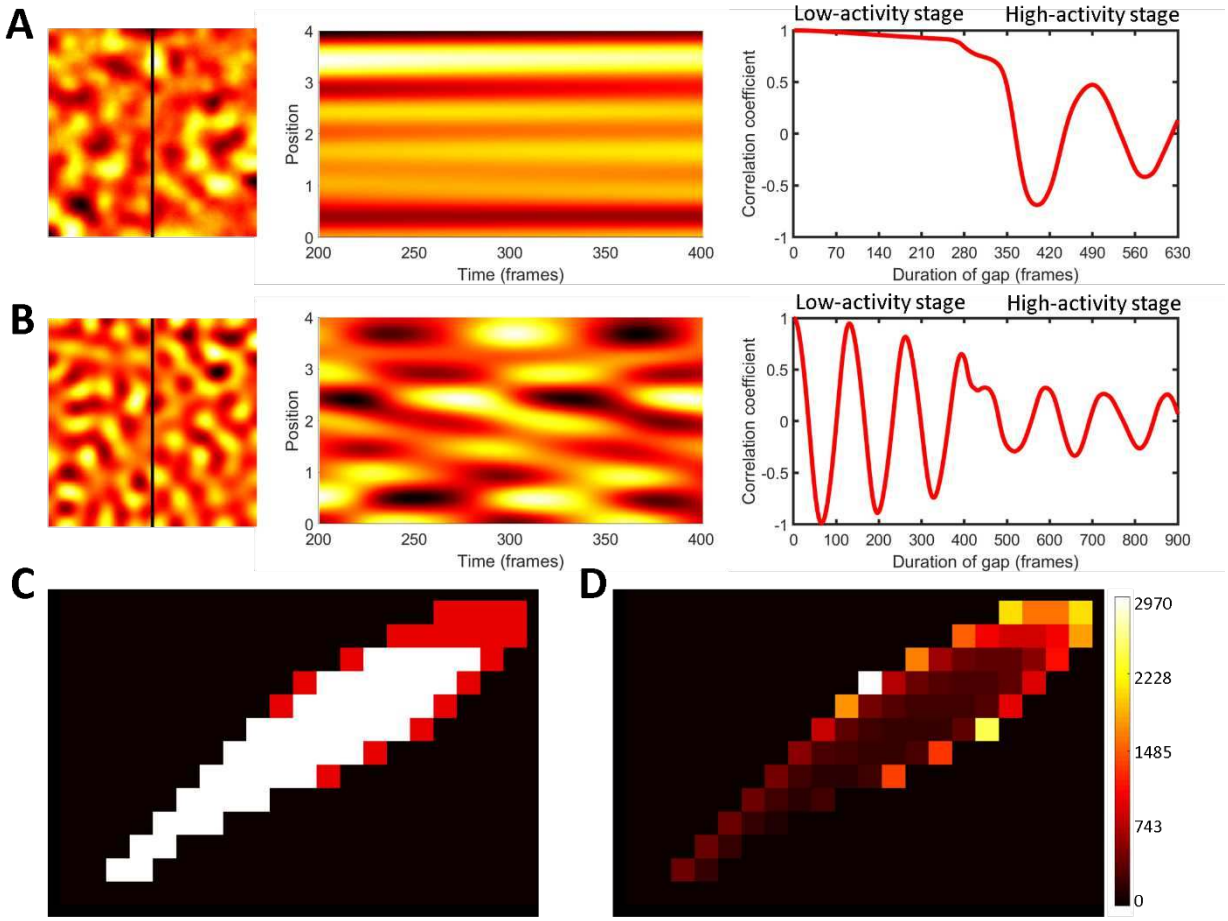

Figure 5. Characteristics of the regimes in the low-activity stage. A, B (Left panels) Snapshots of the system in the quasi-static ($k_0 = 0.2$, $s_2 = 0.8$) and oscillatory ($k_0 = 0.2$, $s_2 = 1.1$) regimes of the low-activity stage; top and bottom panels respectively. (Central panels) Kymograph of the system dynamics along a line shown in black in the left panels. (Right panels) Temporal autocorrelation plots, showing the correlation coefficient as a function of the time lag (see Methods). **C.** Classification of the parameter space with white and red colors indicating the quasi-static and oscillatory regimes, respectively. **D.** Colormap showing the duration of the low-activity stage (in simulation time).

3.5. The directions of the wave vectors are defined during the transition from low- to high-activity stage.

The regimes of the low-activity stage generate different mechanisms of transition to the high-activity stage. In the first case, the system switches the behavior from quasi-static to dynamic (**Fig. 5A**). In the second case, one type of dynamic behavior turns into a different one (**Fig. 5B**). Here we investigate the details of this process. Specifically, we ask what defines the directionality of wave propagation in both cases.

The quasi-static low-activity stage forms periodic patterns that stay spatially fixed while the amplitude of the activity grows. However, during the transition to the high-activity stage, the shape of patterns changes. For low inhibition values (parameter s_2) the system forms *reversed spots* [35]. For intermediate values of inhibition, the system develops *labyrinth-like structures*. Finally, for high values of inhibition, we observe *localized spots* (**Fig. 6A**). These patterns closely resemble the well-known Turing patterns observed, for example, in the Gray-Scott model [13, 36]. Such patterns appear when both activator and inhibitor are co-localized. In **Fig. 6A,** yellow color is produced by merging two channels: green for the activator and red for the inhibitor. Wave propagation is triggered when the activator and inhibitor are spatially displaced relative to each other (**Fig. 6B**). The displacement occurs along the perimeter of the patterns in a periodic manner with the activation patch (green) followed by the inhibitor patch (red). This periodicity leads to the formation of small region of coherent wave-vectors with alternating directions along the Turing-like patterns (**Fig. 6B**). For a longer perimeter of the labyrinth patterns, we see more alignments of the wave-vectors. This alignment explains why wave-domains are observed at an intermediate inhibition strength (**Fig. 3A, C)**, when more complex patterns have high entropy. In contrast, for high and low values of the parameter s_2, spots and reversed sports initiate waves propagating in radial directions toward and outward the centers so that there is no alignment on the larger scale. (**Fig. 6B**).

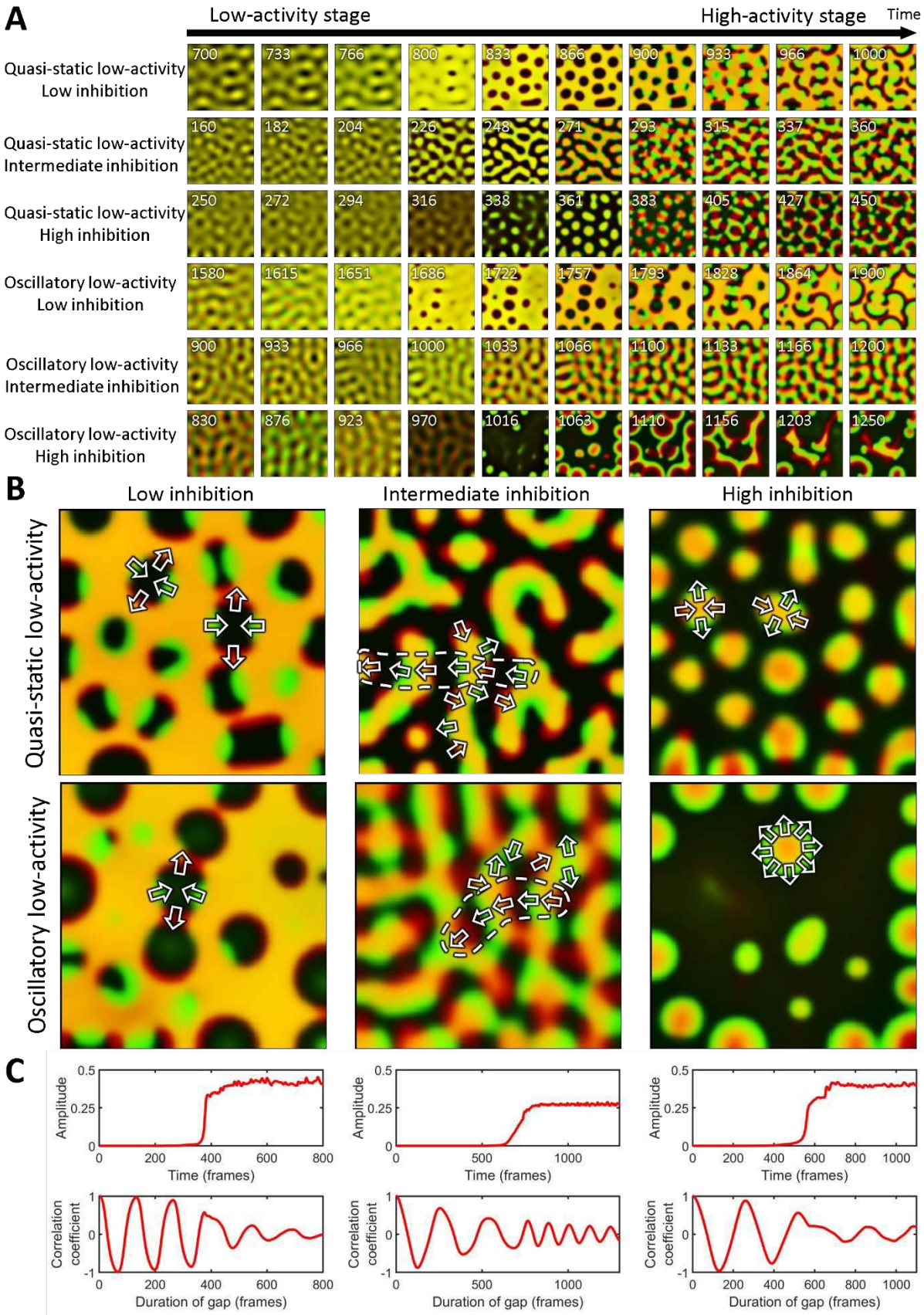
A
Low-activity stage
High-activity stage
Time
Quasi-static low-activity
Low inhibition
700 733 766 800 833 866 900 933 966 1000
Quasi-static low-activity
Intermediate inhibition
160 182 204 226 248 271 293 315 337 360
Quasi-static low-activity
High inhibition
250 272 294 316 338 361 383 405 427 450
Oscillatory low-activity
Low inhibition
1580 1615 1651 1686 1722 1757 1793 1828 1864 1900
Oscillatory low-activity
Intermediate inhibition
900 933 966 1000 1033 1066 1100 1133 1166 1200
Oscillatory low-activity
High inhibition
830 876 923 970 1016 1063 1110 1156 1203 1250
B
Low inhibition
Intermediate inhibition
High inhibition
Quasi-static low-activity
Oscillatory low-activity
C
Amplitude
Time (frames)
Correlation coefficient
Duration of gap (frames)

Figure 6. The transition of the system between the low- and high-activity stages. A. Snapshots of the patterns at low- and high-activity stages for different values of the inhibition strength: (1) weak ($k_0 = 0.18$, $s_2 = 0.7$ for quasi-static and $k_0 = 0.2$, $s_2 = 0.75$ for oscillatory regimes), (2) balanced ($k_0 = 0.2$, $s_2 = 0.9$ for quasi-static and $k_0 = 0.26$, $s_2 = 1.05$ for oscillatory regimes), and (3) strong ($k_0 = 0.22$, $s_2 = 1.1$ for quasi-static and $k_0 = 0.2$, $s_2 = 1.1$ for oscillatory regimes). **B.** Snapshots of the system at the beginning of the high-activity stage. Arrows indicate the direction of wave propagation. Dashed outlines indicate vector alignment on a larger scale. Images in A, B show two merged channels: green for the activator and red for the inhibitor. **C.** The activity amplitude and temporal autocorrelation for the oscillatory low-activity stage with weak negative feedback (left), balanced activation and inhibition (center), and strong negative feedback (right).

Interestingly, during the transition from the oscillatory low-activity stage, the system with weak negative feedback also forms reversed spots but only transiently (**Fig. 6A**). If the negative feedback is strong, the system forms circular waves with the wave-vector pointing in all directions (**Fig. 6B**). In both cases, no wave-domains are observed. However, when activation and inhibition are balanced, the transition between low- and high-activity stages continues smoothly without the formation of any distinct transient patterns (**Fig. 6A**). Consequently, the system with unbalanced activation and inhibition shows a phase-shift in the oscillation upon the transition (left and right panels in **Fig. 6C**), while no phase-shift is observed otherwise (central panels in **Fig. 6C**).

Figure 7A shows regime classification based on the properties of the two stages of pattern development. When the autocatalytic and negative feedbacks are balanced, the total levels of the active and inactive forms of the signaling molecule in the cell are similar to each other so that the activation front and the refractory region are also close in size. This is a situation when patterns of low activity stage are quasi-static, while in the high-activity stage, intermediate values of inhibition lead to the formation of wave domains (the white region in **Fig. 7A**). When both activation (k_0) and inhibition (s_2) are weak (the yellow region in **Fig. 7A**), the system generates large spiral waves with a prolonged front of activation. In the opposite regime, when both activation and inhibition are strong (blue region in **Fig. 7A**), the system operates in the oscillatory regime during the low-activity stage and forms wave domains in the high-activity stage. This regime also has equivalent total levels of the active and inactive form of the molecule. In the border-line regions of the parameter space (green and red regions of **Fig. 7A**), the system forms spiral waves with a larger activation front or a larger refractory region, respectively. Therefore, the balance of feedbacks is the main requirement for the formation of wave domains.

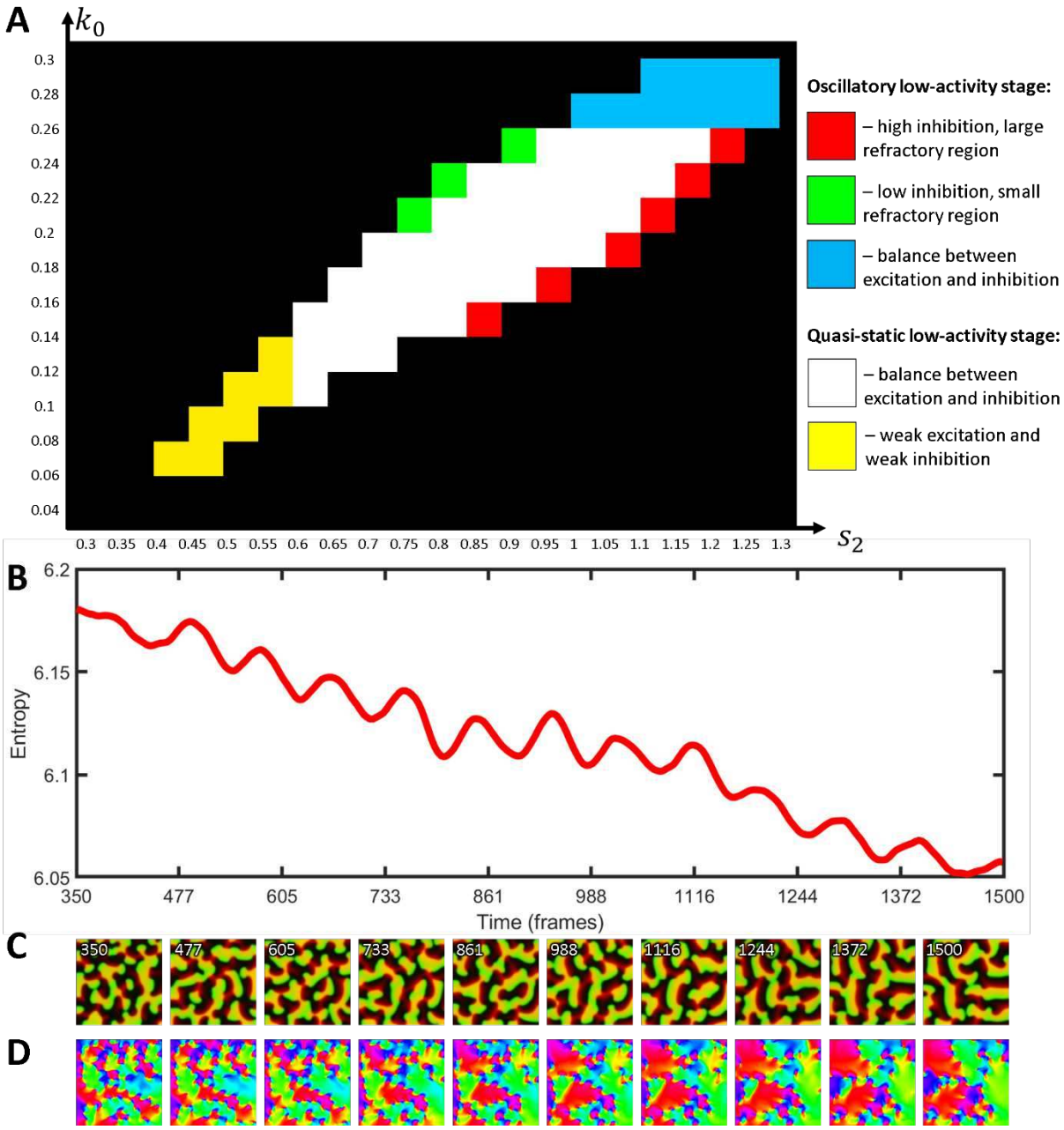

Figure 7. Classification and long-term dynamics of wave domains. A. Different types of system's behaviors in the space of parameters representing the basal activation rate and the strength of negative feedback. **B.** Textural entropy as a function of time during the growth of wave domains ($k_0 = 0.15$, $s_2 = 0.8$). **C.** Snapshots from the simulation in B with the simultaneous visualization of the inhibitor and activator in the system (merged channels). **D.** Colormaps of the direction of wave propagation in C showing the increasing size and decreasing number of the wave domains over time. The values of wave vector angles were averaged with a running window of 100 time steps of the simulation.

It is important to note that once formed, wave domains continue to grow and compete with each other so that the number of domains decreases with time, which is characterized by a gradual decrease in the image entropy (**Fig. 7B**). The shape of the domains also changes. At the beginning of the high-activity stage, they have shapes elongated in the direction of the wave vector. Over time, wave domains become wider and acquire a cone-like shape (**Fig. 7C, D**). In the experimental data [25] on starfish oocytes, we also see the progressive increase of the domain sizes (**Supplemental Video 1**). However, this process does not continue long enough to see a single wave domain winning the whole area because mitosis resets the dynamics. In summary, all the apparent features of the wave domains in our simulations are consistent with the experimental observations that motivated this work.

3.6. Simulations with high values of intrinsic noise capture the cortical actin dynamic in frog embryos.

Sufficiently high values of noise (e.g., $\alpha_1 = 3, \alpha_2 = 0.1$) alter system's behavior described in the previous sections. While for some parameters we still see the formation of wave domains (e.g., $k_0 = 0.19,\ s_2 = 0.9$), for other parameters (e.g., $k_0 = 0.25,\ s_2 = 1.25$) large noise can lead to the formation of disjoined patches of activation. Such dynamics closely resembles actin waves in the cortex of frog (*Xenopus laevis*) oocytes [25] and frog blastomeres in our experiments. **Figure 8A** shows an example of patterns of active Rho in starfish oocyte [25], F-actin in frog blastomere, and both active Rho and F-actin signals from our simulations corresponding to these cell types. For quantitative comparison of experimental and simulated data, we characterized the patterns with a set of textural measures (see Methods) and used PCA analysis to show the similarity of the patterns (**Fig. 8B**).

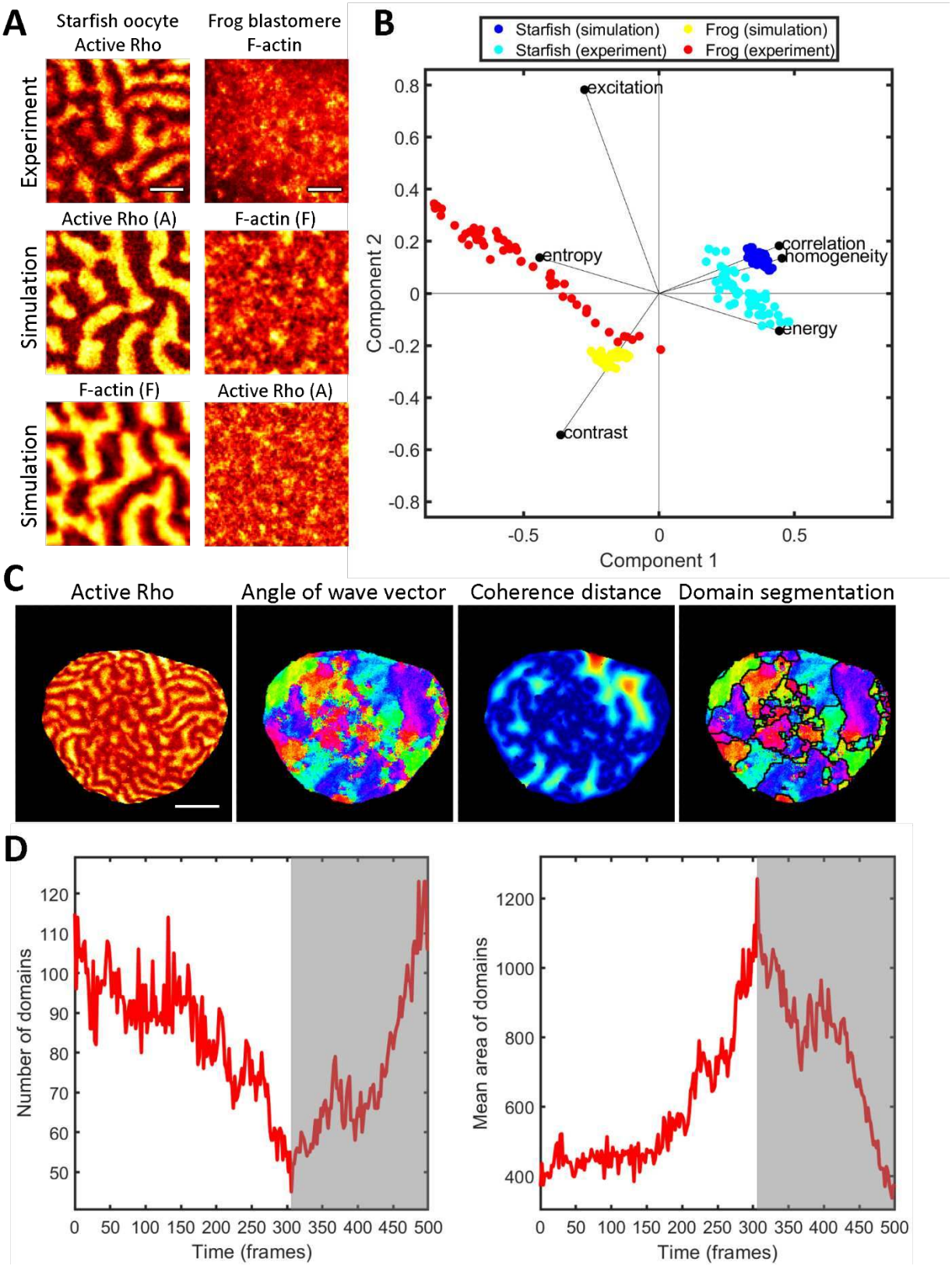

Figure 8. Quantitative analysis of active Rho and F-actin patterns in experimental data and simulation. A. An example of starfish (active Rho) and frog (F-actin) cortical dynamics with the corresponding simulation results representing both active Rho

and F-actin signals. The scale bar is 20 μm. **B.** Biplot representing the results of PCA analysis of simulation and experimental data. Active Rho signal was used for starfish data and F-actin for frog data. 50 consecutive frames were used from each dataset for the analysis. **C.** The pipeline of wave domain identification in starfish images, including active Rho pattern, colormap of wave vector directions, colormap of the coherence distance, and wave domain segmentation. The scale bar is 50 μm. **D.** The mean size of wave domains as a function of time for starfish oocyte. The grey area indicates the period of time after the sharp switch in the cell behavior.

In addition to the textural characterization, we also applied our automated method of wave-domain detection to the starfish experimental data. **Figure 8C** illustrates the processing pipeline, which includes computing and averaging the wave vector angles, finding the coherence distance, and segmenting it to extract regions of coherent wave propagation (see **Methods**). In agreement with our definition, regions are identified as wave domains if their size is larger than the width of activation front. The lifetime of these wave domains is also larger than the period of oscillation. The initial stage is consistent with the simulation results showing the growth of wave domains' size and decrease in the number of wave domains (compare **Fig. 2H and Fig. 8D**). However, in the later part of the experimental record during anaphase, the systems behavior changes abruptly (gray areas in **Fig. 8D**). The dynamics reverse into increasing the number of wave domains and decreasing the size of domains until the waive propagation completely ceases. Although our model is not built to capture this dynamic reversal, our method of wave domain identification allows us to pinpoint the moment of time when some biological process triggered the change in the system behavior. This behavioral switch could be related to a change in the rate of CDK1 activity and the rearrangement of cortical microtubules, which may impact the actin dynamics/Rho activity in the oocyte.

4. Discussion

Wave domains of actin polymerization and active Rho in the cortex of starfish oocytes may appear as a subtle feature of the cytoskeletal regulation. However, this behavior emerges from a complex intertwined signaling network, and the ability of a computational model to accurately capture such a phenomenon is important for the mechanistic understanding of the underlying processes. In this work, we showed that the development of wave domains has a non-trivial temporal progression. Before wave domains become clearly visible, the system goes through a period of pattern formation with activity level orders of magnitude smaller than the activity at the later stage, the stage that we can compare with the experimental observations of Bement *et al.* [25]. Interestingly, types of patterns in this low-activity stage and the way they become destabilized determines whether we see spiral waves or wave domains. Specifically, wave domains emerge in two cases: (1) when the low-activity patterns are spatially static, have the labyrinth-like organization, and become destabilized through a displacement of the activator and inhibitor peaks along the perimeter of the pattern shapes, and (2) when the low-activity patterns are oscillatory and the transition to high-activity patterns occurs with the preservation of the oscillation phase. In both cases, the strengths of the basal activation and negative feedback have to be balanced so that the total levels of the active and inactive forms of the regulator (e.g., Rho GTPase) are close to each other. In addition to the unstable homogeneous state in the presence of limit cycle, this balance becomes a necessary requirement for the emergence of the observed wave dynamics. If the balance is broken and the activation starts to dominate over inhibition or vice versa, the wave domains are not formed and instead we see spiral waves.

We make clear distinction between spiral waves and the wave domains by representing Rho activity with a spatiotemporal map of the wave-vector directions and applying our segmentation pipeline for automatic detection of the wave domain outlines. In wave domains, the directions are coherent and parallel to the long sides of the domain. When the domains are adjacent to each other at their long side, the waves propagate in opposite directions parallel to the interface between the domains. As opposed to spiral waves, wave domain formation is a higher level of complexity as indicated by the higher textural entropy of the dynamic patterns. Furthermore, in the high-activity stage, the dynamics continues to transform so that domains slowly increase in size and decrease in number. Therefore, in this work, even though we characterized different stages of pattern development, we always dealt with transient dynamics. The experimentally

observed dynamics is also transient in the sense that it occurs only during a part of the cell cycle, after the beginning of anaphase and before the formation of cytokinetic furrow.

Intriguingly, quantifying wave domains characteristics (their sizes and number) over time revealed that, in starfish oocytes, the development of the wave domains agrees with the model up to a point of a sharp dynamic reversal. Some cell-cycle event triggers the switch from increasing the size of the wave domains to decreasing them until the wave propagation stops as cell enters mitosis. The presence of such event was not apparent from the visual inspection but became evident with the quantification of wave domains (**Fig 8D**). This result emphasizes the power of the concept of wave domains, which serves as a characteristic feature for comparative analysis of the very complex wave dynamics evolving over time on the whole cell level.

We also showed that accounting for intrinsic noise is critical for capturing a range of possible dynamic behaviors in different model organisms or, potentially, in the same organism but under different perturbations. We described the effects of the strong noise on the pattern formation and showed that our model quantitatively reproduces wave dynamics in both starfish and frog cells. The model predicts that the difference between two regimes is attributed to changes in both the activation rate of Rho GTPase and the strength of negative feedback from F-actin.

In this report, we quantitatively characterized spatiotemporal patterns using textural measures, autocorrelations plots, and our novel tool for wave domain detection, but we only scratch the surface of this overlooked phenomenon. In future studies, experimental perturbations that affect either the autocatalytic or negative feedback in the Rho signaling motif could disturb the feedback balance enough to shift the system into different dynamic regimes predicted by the model. This, in turn, could provide an insight into the role of different signaling components in the cytoskeletal regulation. Our results indicate that, in addition to the regulation of Rho activation (e.g., through Ect2, which is a GEF for Rho GTPase [25]), the negative feedback from F-actin plays a key role in regulating the activity patterns, although the molecular mechanisms involved in this feedback are not understood yet. A biological role of the wave domain formation also remains to be investigated.

In future studies, the biological community can benefit from our automated wave detection methodology because it is a novel characteristic, which is more intuitive than a set of textural measures, such as image entropy, correlation, and energy. If wave domains are present in a set of imaging data, the statistics of their sizes, shapes, and numbers describes the *geometric* structure of the wave patterns, that can be used to explain subtle differences in cell dynamics under different perturbations or under different natural conditions during the cell cycle.

Methods

Reaction-diffusion model of Rho GTPases activity

For this study, we have built a two-dimensional reaction-diffusion model based on a one-dimensional version by Holmes *et al.* [24]. GTPase kinetics is represented with the mass-conserved activator-substrate (MCAS) motif that describes switching between the active (GTP-bound) and inactive (GDP-bound) forms with autocatalytic feedback presumably through guanine nucleotide exchange factors (GEFs). The negative feedback depends on F-actin, which is polymerized in response to the activation of nucleation-promoting factors downstream of Rho signaling. F-actin suppresses Rho activity through a mechanism, which is not fully understood but is assumed in multiple studies [24, 25, 37]. The minimal signaling model for such a process can be represented as a three-component system:

$$\frac{\partial A}{\partial t} = f + D_A \frac{\partial^2 A}{\partial x^2} + D_A \frac{\partial^2 A}{\partial y^2} + \alpha_1 \xi_1 \quad (1)$$

$$\frac{\partial I}{\partial t} = -f + D_I \frac{\partial^2 I}{\partial x^2} + D_I \frac{\partial^2 I}{\partial y^2} - \alpha_1 \xi_1 \quad (2)$$

$$\frac{\partial F}{\partial t} = k_n A - k_s F + \alpha_2 \xi_2 \tag{3}$$

where

$$f = \left(k_0 + \gamma \frac{A^3}{{A_0}^3 + A^3}\right) I - \left(s_1 + s_2 \frac{F}{F_0 + F}\right) A \tag{4}$$

and

$$D_A = \frac{0.001}{3}, D_I = \frac{0.1}{3}, k_0 \in [0, 0.3], \gamma = 1, A_0 = 0.4,$$

$$s_1 = 0.5, s_2 \in [0, 1.3], F_0 = 0.5, k_n = 0.1, k_s = 0.025, \alpha_{1,2} \in [10^{-15}, 3]$$

Here, we refer to A, I, and F as active and inactive forms of a GTPase (or a GEF, or a nucleation-promoting factor in other contexts) and F-actin, for consistency with the experimental study of Rho activity [25] and the original notations in [24]. Component A diffuses slowly on the membrane. Its autocatalytic activation is represented with the Hill function $\gamma \frac{A^3}{{A_0}^3 + A^3}$. Component I diffuses fast in the cytosol. Our model does not account for spatial translocation of actin mesh, so component F has zero diffusion. The negative feedback from F-actin is represented with the Hill function: $s_2 \frac{F}{F_0 + F}$. The activation and deactivation terms also include constant basal rates, k_0 and s_1, respectively. The total amount of A and I is conserved, so that the model does not account for changes in GTPase expression level and is suitable for fast processes within the cell cycle.

We solve the partial differential equations (1-3) using the Euler method (Eq. 5) with time step $\Delta t = 0.001$ and spatial step $h = 0.02$. To implement no-flux boundary conditions for an arbitrary cell shape, we applied the modified five-point stencil of the 2D Laplace operator $L^t_{i,j}$, so that:

$$C^{t+1}_{i,j} = C^t_{i,j} + \Delta t \left\{ f^t_{i,j} + \frac{D_C}{h^2} L^t_{i,j} \right\} \tag{5}$$

$$L^t_{i,j} = M_{i+1,j}\left(C^t_{i+1,j} - C^t_{i,j}\right) - M_{i-1,j}\left(C^t_{i,j} - C^t_{i-1,j}\right) \tag{6}$$
$$+ M_{i,j+1}\left(C^t_{i,j+1} - C^t_{i,j}\right) - M_{i,j-1}\left(C^t_{i,j} - C^t_{i,j-1}\right)$$

where $C^t_{i,j}$ is the concentration in position (i, j) at time t, M is the binary mask representing the cell ($M_{i,j} = 1$) and the background ($M_{i,j} = 0$), D_C is the diffusion coefficient, and f is the reaction term (Eq. 4). The discrete Laplace operator $L^t_{i,j}$ consists of four fluxes. For boundary pixels of the cell mask, the fluxes to the adjacent pixels of the background are multiplied by $M_{i,j} = 0$, thus, ensuring no loss of concentration through the boundary. In the case of a square domain, we used masks of various sizes (202x202 and 512x512) with one-pixel-wide padding to define the background. The solution was saved every 1000 iterations.

Eqs. (1-3) also include noise terms generated as Gaussian random numbers, ξ_1 and ξ_2, with zeros mean and the standard deviation of one, so that $\alpha_{1,2}$ is the magnitude of the noise. These terms represent random fluctuations in the number of the molecules within the cell area of one pixel. Since the total number of GTPase molecules in the cell is assumed constant, the noise contributions to the equations for A and I have opposite signs. If added noise brings low concentration to a negative value, it is reset to zero on the next iteration. In our simulations, noise with $\alpha_1 = \alpha_2 = 10^{-15}$ was sufficient to initiate wave propagation from the unstable homogeneous state. We also used higher magnitudes to reproduce the noisy dynamics in the starfish ($\alpha_1 = \alpha_2 = 2$, **Fig. 1A**) and our frog ($\alpha_1 = 3, \alpha_2 = 0.1$, **Fig. 8A**) data. The described implementation of the PDE solution is available at [https://github.com/tsygankov-lab/WaveDomains].

Characterization of system's dynamics over the course of pattern development

To visualize patterns with the amplitude growing exponentially from a homogeneous state, we scaled the solution as $A_{scaled} = \frac{A-\min(A)}{\max(A)-\min(A)}$. For kymographs representing the dynamics of the system across the secant line of the domain, the solution was scaled as $A_{scaled} = \frac{A-\mathrm{mean}(A)}{\mathrm{std}(A)}$ to show the normalized deviation of the concentration from the mean value. The duration of the stage of rapid amplitude growth, T_g, was measured as the period of linear increase in the log-transformed amplitude $a_l(t) = \log\left(\max_{i,j}(A^t) - \min_{i,j}(A^t)\right)$, such that $\left|\frac{d}{dt}a_l(t)\right| > 0.001$.

Temporal autocorrelation analysis

To analyze pattern dynamics, we used temporal autocorrelation using Pearson's linear correlation (see **Supplemental Figure S3A**) coefficient as:

$$C^t(\tau) = \underset{i,j}{\mathrm{corr}}\left(A^t_{i,j}, A^{t+\tau}_{i,j}\right) = \frac{\sum_{i,j\in D}\left(A^t_{i,j}-\bar{A}^t\right)\left(A^{t+\tau}_{i,j}-\bar{A}^{t+\tau}\right)}{\sqrt{\sum_{i,j\in D}\left(A^t_{i,j}-\bar{A}^t\right)^2 \cdot \sum_{i,j\in D}\left(A^{t+\tau}_{i,j}-\bar{A}^{t+\tau}\right)^2}}.$$

Here, the pattern at time t, $A^t_{i,j}$, is compared with the pattern after a time lag τ, $A^{t+\tau}_{i,j}$, and $\bar{A}^t$ is the average value of A at time t over the whole simulation domain D. Next, we plot the correlation coefficients as functions of the time lag τ. In the case of quasi-static behavior, the temporal autocorrelation coefficient is close to a constant value of one, while in the case of oscillatory behavior, it exhibits periodic oscillations. A regime was classified as oscillatory if the difference between the maximum and minimum values of the temporal autocorrelation coefficient in the window $\tau \in [0.5T_g, 0.9T_g]$ was bigger than one:

$$\max_{\tau} C^t(\tau) - \min_{\tau} C^t(\tau) > 1.$$

Quantitative analysis of wave propagation using textural features

To compare regimes of wave propagation, we applied the following texture analysis. The experimental data was preprocessed with ImageJ [38] to crop the frame of cell cortex of 87x87 μm. The experimental and simulation data was then resized to have identical resolution of 100x100 pixels. Within the time window that was used for the analysis, the data was scaled as $A_{scaled} = \frac{A-\mathrm{mean}(A)}{\mathrm{std}(A)}$. The image entropy was computed with the MATLAB function *entropy*. The image contrast, correlation, energy, and homogeneity were computed with the function *graycoprops(GCM)*, where the gray-level co-occurrence matrix GCM was computed with the function *graycomatrix*. We also used a measure of the excitation level, which was computed as the fraction of the area, where the concentration of the activator is higher than its mean value. The dimensionality reduction and visualization were performed with the MATLAB functions *pca* and *biplot*.

Characterization of the spatial distribution of the direction of wave vectors.

To compute wave vectors from the time-series data, we compared the state of the system at each pixel (x_i, y_i) at time t with the pixels (x_j, y_j) in the convolution window W around the pixel (x_i, y_i) at time $t + \tau$. The similarity of pixel (x_i, y_i) with pixels (x_j, y_j) was computed based on the difference in the concentration $|A^t_{x_i,y_i} - A^{t+\tau}_{x_j,y_j}|$ and in the spatial Sobel gradient $\left|\mathrm{grad}\left(A^t_{x_i,y_i}\right) - \mathrm{grad}\left(A^{t+\tau}_{x_j,y_j}\right)\right|$ (see **Supplemental Figure S3B**). Thus, we defined the wave-vector as a weighted sum of vectors pointing from (x_i, y_i) to (x_j, y_j):

$$\vec{k}(x_i, y_i) = \sum_{j \in W} \frac{\vec{v}(x_j, y_j) - \vec{v}(x_i, y_i)}{\left(1 + \left|A^{t+\tau}_{x_j, y_j} - A^{t}_{x_i, y_i}\right| + \left|\mathrm{grad}\left(A^{t+\tau}_{x_j, y_j}\right) - \mathrm{grad}\left(A^{t}_{x_i, y_i}\right)\right|\right)^5}.$$

For our simulated data with a small value of noise ($\alpha = 10^{-15}$), we used 5-pixel convolution window and the time lag $\tau = 8$. The computed values of wave vector angles, θ, were averaged with the running window of 300 frames. For the analysis of starfish oocyte data, we used 5-pixel convolution window and $\tau = 1$ frame (19 seconds) and time averaging over 15 frames. The average values were computed using the circular mean [33]. For the visualization, we plotted the angles, θ, for each image pixel with the cyclic HSV (hue, saturation, and value) colormap, which generates the same color for the lowest value of the colormap (zero) as for its highest value (2π). To visualize the magnitude of a local change in the direction of wave vectors, θ, we used Sobel gradient of the image of values ($\sin\theta + \cos\theta$). Finally, for the analysis of experimental data with moving cell edge, we extracted the overlapping part of cell masks within the averaging time window.

Frog embryo, microinjection, and microscopy

Ovulation of *Xenopus laevis* was induced by injecting 0.5ml Chorionic Gonadotrophin (1,000U/ml, Sigma) into the dorsal lymph sac of the female animal the night before. On the second day, eggs were gently squeezed into a petri dish and mixed with a small piece of testes isolated from male frogs. After fertilization, eggs were dejellied in 3% cysteine in 0.1x MMR (Marc's Modified Ringer's, 100mM NaCl, 2mM KCl, 2mM $CaCl_2$, 1mM $MgCl_2$, 5mM HEPES, pH7.4) and washed in 0.1x MMR. For microinjection, embryos were changed into 3% Ficoll solution in 0.5x MMR. Embryos were injected at 1-2 cell stage with 1ng of Cherry-LifeAct RNA into the animal pole. Injected embryos were maintained at 18C for 2-3 hours till they reached stage 6 (32-cell stage), before vitelline membrane was carefully removed by a pair of forceps. The embryos were then mounted into glass bottom dish filled with 0.1x MMR and positioned with animal pole facing the cover glass. The embryos were hold into position by a small piece of cover glass raised by a ring of silicone grease. Imaging was acquired with PerkinElmer Spinning Disk Confocal microscope using a 60x objective. Around 4um z-stacks were captured at 2.5 seconds intervals for 10 minutes.

All protocols in this study were carried out in accordance with the recommendations of United States Department of Agriculture (USDA) Animal Welfare Act Regulations and Public Health Service Policy and is approved by Georgia Institute of Technology Institutional Animal Care and Use Committee (IACUC number A100001) and Georgia Institute of Technology Biosafety Committee (IBC number R18021). The present animal investigation was conducted in consideration of the National Institutes of Health guide for the care and use of Laboratory animals (NIH Publications No. 8023, revised 1978) and complied with the ARRIVE guidelines.

Data Availability

https://github.com/tsygankov-lab/WaveDomains

Author Contributions

D.T., S.N., and S.H. designed the study. D.T. performed project administration and supervision. S.H. developed the model, performed simulations, and analyzed data. S.N. and M.K. performed experiments and collected imaging data. D.T. and S.H. wrote the manuscript and prepared figures/videos. S.N. and M.K. contributed to manuscript discussion and editing.

Conflict of Interest

The authors declare that the research was conducted in the absence of any commercial or financial relationships that could be construed as a potential conflict of interest.

Acknowledgements

The authors would like to acknowledge the Partnership for an Advanced Computing Environment (PACE) at Georgia Tech for the provided computational resources.

Funding

This work was supported by grants from the U.S. Army Research Office (ARO, W911NF-17-1-0395) and the National Science Foundation (CMMI 1942561) to D.T., and by the National Institutes of Health (R01GM136892) to S.N and D.T.

Supplementary Material

1. Supplemental Information with Figures S1-S3 in a single PDF file.
2. Supplemental Videos S1-S6

Supplemental Video Captions

Video S1. Spatiotemporal distribution of Rho activity in the starfish oocyte experiment of Bement *et al.* (left) and our simulation model (right).

Video S2. The result of a series of simulations for different values of parameters k_0 (vertical axes) and s_2 (horizontal axis) with nonhomogeneous initial conditions (a spike of activity in the center).

Video S3. The results of a series of simulations for different values of parameters k_0 (vertical axes) and s_2 (horizontal axis) with homogeneous initial conditions.

Video S4. A simulation of wave formation from homogeneous initial conditions in the quasi-static regime of the low-activity stage for a weak inhibition ($k_0 = 0.15$, $s_2 = 0.6$).

Video S5. A simulation of wave formation from homogeneous initial conditions in the quasi-static regime of the low-activity stage for a balanced (intermediate) inhibition ($k_0 = 0.2$, $s_2 = 0.9$).

Video S6. A simulation of wave formation from homogeneous initial conditions in the oscillatory regime of the low-activity stage for a strong inhibition ($k_0 = 0.2$, $s_2 = 1$).

References

1. Hodge, R.G. and A.J. Ridley, *Regulating Rho GTPases and their regulators.* Nat Rev Mol Cell Biol, 2016. **17**(8): p. 496-510.
2. Ridley, A.J., *Rho GTPases and actin dynamics in membrane protrusions and vesicle trafficking.* Trends Cell Biol, 2006. **16**(10): p. 522-9.
3. Machacek, M., et al., *Coordination of Rho GTPase activities during cell protrusion.* Nature, 2009. **461**(7260): p. 99-103.
4. Marston, D.J., et al., *Multiplexed GTPase and GEF biosensor imaging enables network connectivity analysis.* Nat Chem Biol, 2020. **16**(8): p. 826-833.
5. Komatsu, N., et al., *Development of an optimized backbone of FRET biosensors for kinases and GTPases.* Mol Biol Cell, 2011. **22**(23): p. 4647-56.
6. Guan, X., et al., *Rho GTPases and related signaling complexes in cell migration and invasion.* Exp Cell Res, 2020. **388**(1): p. 111824.
7. Turing, A.M., *The chemical basis of morphogenesis. 1953.* Bull Math Biol, 1990. **52**(1-2): p. 153-97; discussion 119-52.

8. Tyson, J.J. and J.D. Murray, *Cyclic AMP waves during aggregation of Dictyostelium amoebae.* Development, 1989. **106**(3): p. 421-6.
9. Meinhardt, H., *Orientation of chemotactic cells and growth cones: models and mechanisms.* J Cell Sci, 1999. **112 (Pt 17)**: p. 2867-74.
10. Murray, J.D., *Mathematical biology*. 3rd ed. ed. Interdisciplinary applied mathematics. 2002, New York: Springer.
11. FitzHugh, R., *Mathematical models of threshold phenomena in the nerve membrane.* The bulletin of mathematical biophysics, 1955. **17**(4): p. 257-278.
12. Nagumo, J., S. Arimoto, and S. Yoshizawa, *An active pulse transmission line simulating nerve axon.* Proceedings of the IRE, 1962. **50**(10): p. 2061-2070.
13. Cross, M.C. and P.C. Hohenberg, *Pattern formation outside of equilibrium.* Reviews of Modern Physics, 1993. **65**(3): p. 851-1112.
14. Belousov, B.P., *A periodic reaction and its mechanism.* Oscillation and Travelling Waves in Chemical Systems, 1951.
15. Mori, Y., A. Jilkine, and L. Edelstein-Keshet, *Wave-pinning and cell polarity from a bistable reaction-diffusion system.* Biophys J, 2008. **94**(9): p. 3684-97.
16. Goryachev, A.B. and M. Leda, *Compete or Coexist? Why the Same Mechanisms of Symmetry Breaking Can Yield Distinct Outcomes.* Cells, 2020. **9**(9).
17. Chiou, J.G., et al., *Principles that govern competition or co-existence in Rho-GTPase driven polarization.* PLoS Comput Biol, 2018. **14**(4): p. e1006095.
18. Otsuji, M., et al., *A mass conserved reaction-diffusion system captures properties of cell polarity.* PLoS Comput Biol, 2007. **3**(6): p. e108.
19. Simon, C.M., et al., *Pattern formation of Rho GTPases in single cell wound healing.* Mol Biol Cell, 2013. **24**(3): p. 421-32.
20. Goryachev, A.B. and A.V. Pokhilko, *Dynamics of Cdc42 network embodies a Turing-type mechanism of yeast cell polarity.* FEBS Lett, 2008. **582**(10): p. 1437-43.
21. Kuo, C.C., et al., *Inhibitory GEF phosphorylation provides negative feedback in the yeast polarity circuit.* Curr Biol, 2014. **24**(7): p. 753-9.
22. Goryachev, A.B., et al., *How to make a static cytokinetic furrow out of traveling excitable waves.* Small GTPases, 2016. **7**(2): p. 65-70.
23. Meinhardt, H. and A. Gierer, *Pattern formation by local self-activation and lateral inhibition.* Bioessays, 2000. **22**(8): p. 753-60.
24. Holmes, W.R., A.E. Carlsson, and L. Edelstein-Keshet, *Regimes of wave type patterning driven by refractory actin feedback: transition from static polarization to dynamic wave behaviour.* Phys Biol, 2012. **9**(4): p. 046005.
25. Bement, W.M., et al., *Activator-inhibitor coupling between Rho signalling and actin assembly makes the cell cortex an excitable medium.* Nat Cell Biol, 2015. **17**(11): p. 1471-83.
26. Voit, E.O., *A first course in systems biology*. 2013, New York: Garland Science.
27. Strogatz, S.H., *Nonlinear dynamics and chaos : with applications to physics, biology, chemistry, and engineering*. Second edition. ed. 2015, Boulder, CO: Westview Press, a member of the Perseus Books Group.
28. Majumder, R., et al., *Optogenetics enables real-time spatiotemporal control over spiral wave dynamics in an excitable cardiac system.* Elife, 2018. **7**.
29. Fukujin, F., et al., *Self-organization of chemoattractant waves in Dictyostelium depends on F-actin and cell-substrate adhesion.* J R Soc Interface, 2016. **13**(119).
30. Taniguchi, D., et al., *Phase geometries of two-dimensional excitable waves govern self-organized morphodynamics of amoeboid cells.* Proc Natl Acad Sci U S A, 2013. **110**(13): p. 5016-21.
31. La Porta, A. and C.M. Surko, *Predicting the motion of phase defects in a traveling-wave convection pattern.* Physica D: Nonlinear Phenomena, 2000. **139**(1): p. 177-185.
32. Loose, M., et al., *Spatial regulators for bacterial cell division self-organize into surface waves in vitro.* Science, 2008. **320**(5877): p. 789-92.

33. Berens, P., *CircStat: A MATLAB Toolbox for Circular Statistics.* 2009, 2009. **31**(10): p. 21.
34. Meyer, F., *Topographic Distance and Watershed Lines.* Signal Processing, 1994. **38**(1): p. 113-125.
35. Shoji, H., Y. Iwasa, and S. Kondo, *Stripes, spots, or reversed spots in two-dimensional Turing systems.* J Theor Biol, 2003. **224**(3): p. 339-50.
36. Kondo, S. and T. Miura, *Reaction-diffusion model as a framework for understanding biological pattern formation.* Science, 2010. **329**(5999): p. 1616-20.
37. Miao, Y., et al., *Wave patterns organize cellular protrusions and control cortical dynamics.* Mol Syst Biol, 2019. **15**(3): p. e8585.
38. Schneider, C.A., W.S. Rasband, and K.W. Eliceiri, *NIH Image to ImageJ: 25 years of image analysis.* Nat Methods, 2012. **9**(7): p. 671-5.

Figures

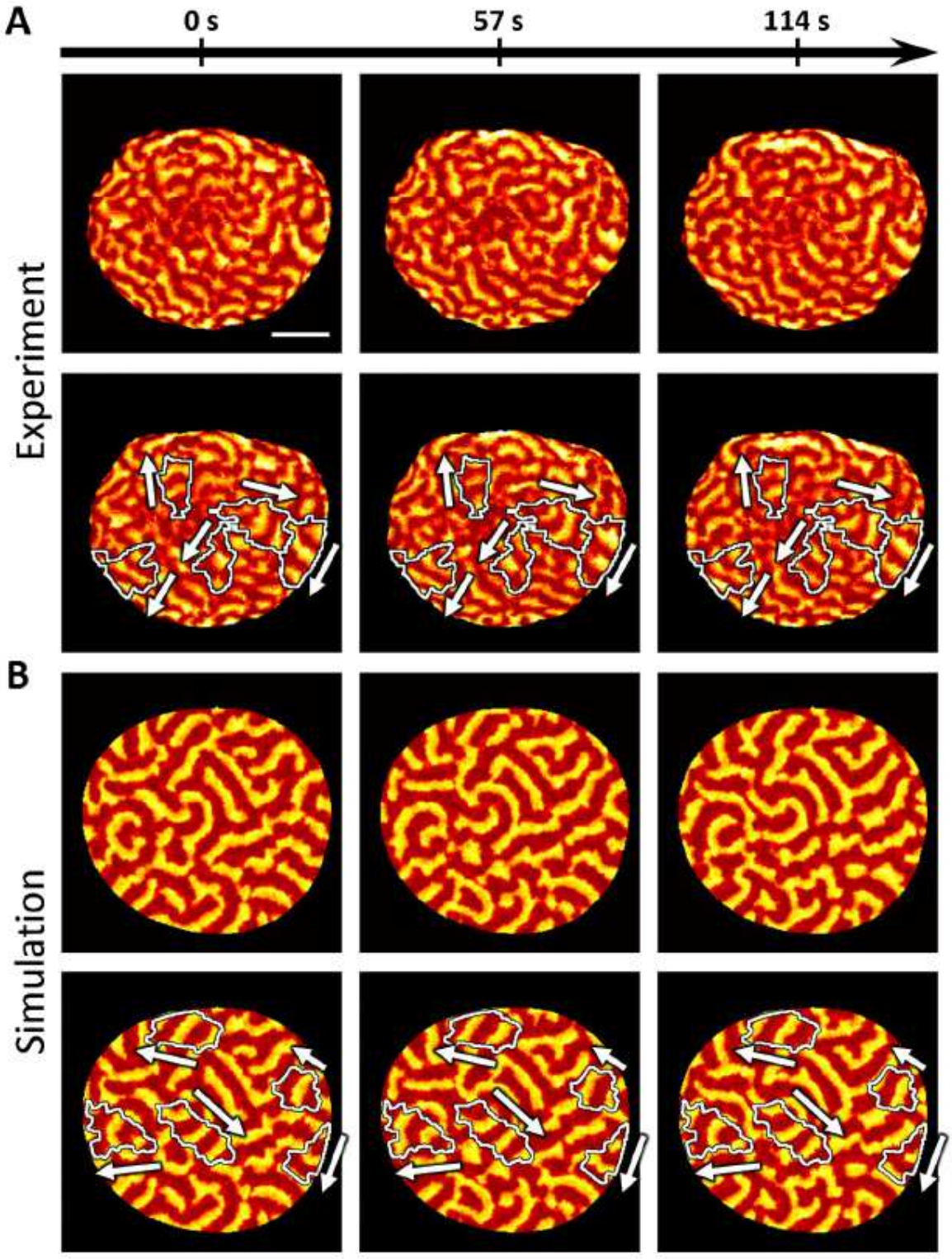

Figure 1

Cortical waves of Rho activity in Patiria miniata oocytes during anaphase before the formation of cytokinetic furrow. Both the experiment [25] and our model show similar overall dynamics and the presence of wave domains. A. Snapshots of wave propagation in the experiment [25]. The scale bar is 50

μm. B. Snapshots of wave propagation in our simulation (□□0=0.2, □□2=1,□□1,2=2). The white contours outline wave domains as defined in the following section, while the arrows indicate the direction of wave propagation in these domains. For the full dynamics see Supplemental Video 16 in [25] and Supplemental Video 1.

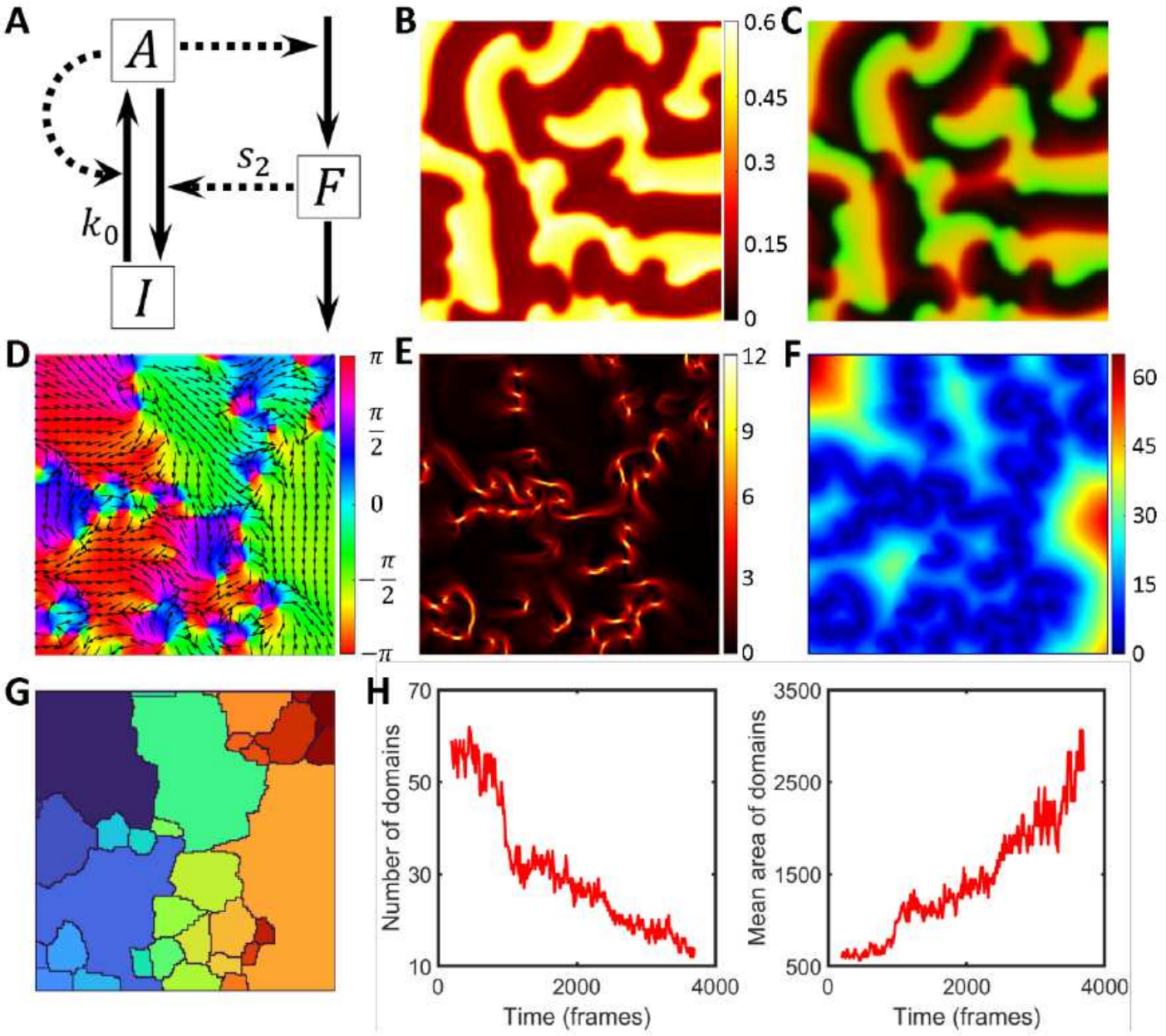

Figure 2

See manuscript for full figure caption.

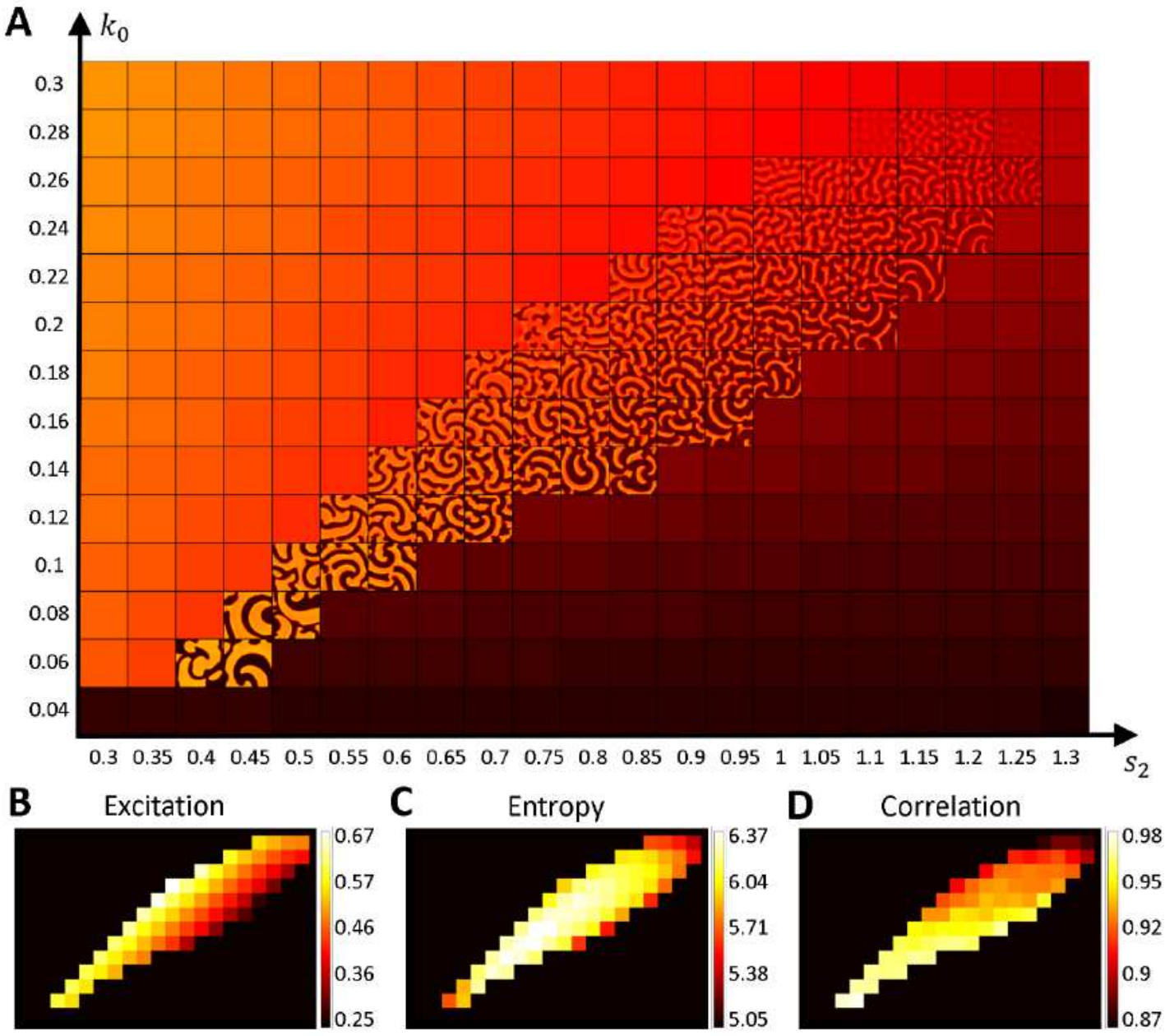

Figure 3

Parameter scan and textural analysis of the emerging patterns. A. The result of model simulations for a range of parameters ⍰⍰0 and ⍰⍰2 (see also Supplemental Video 3). B. The colormap of the excitation measure (see Methods) for the parameter space in A. C, D. The textural measures of pattern entropy and correlation for the parameter space in A. Each measure was averaged over 100 simulation steps after the formation of waves from the initial homogeneous state.

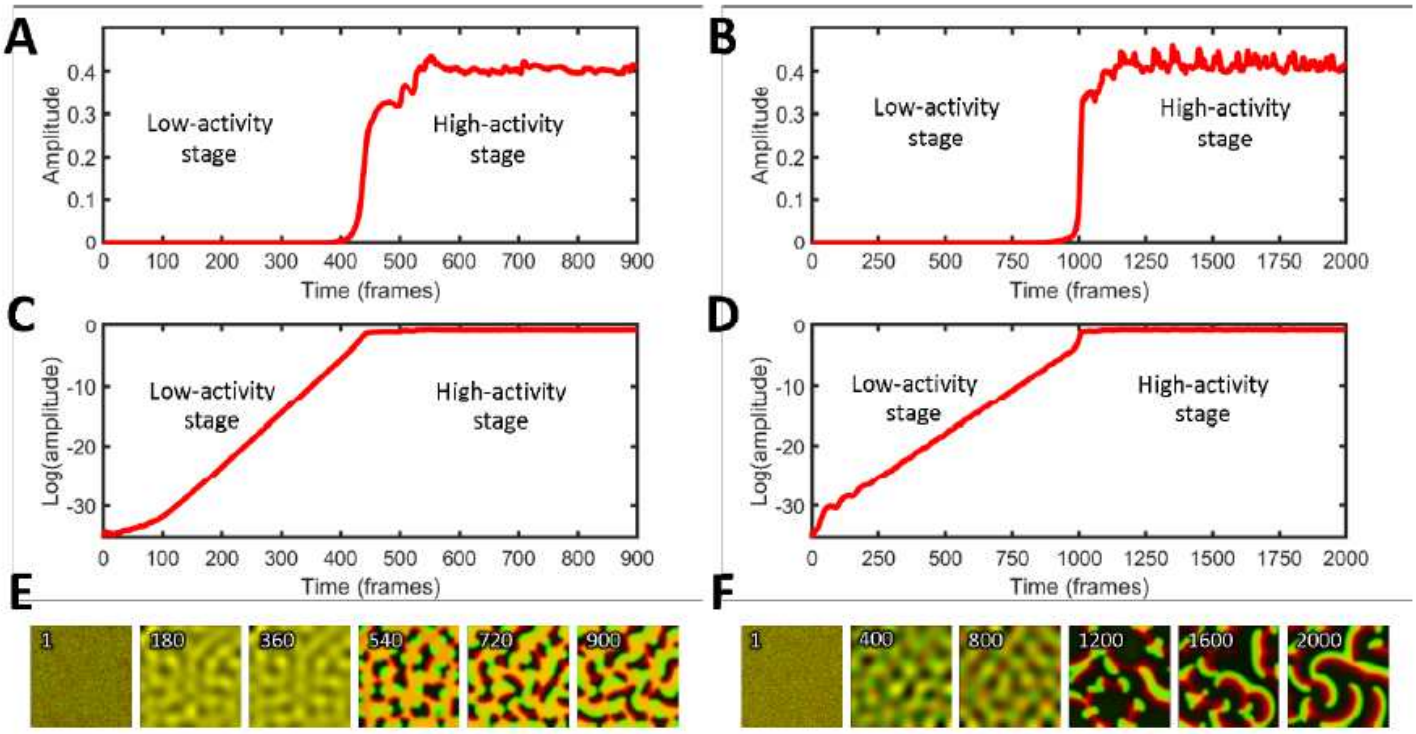

Figure 4

See manuscript for full figure caption.

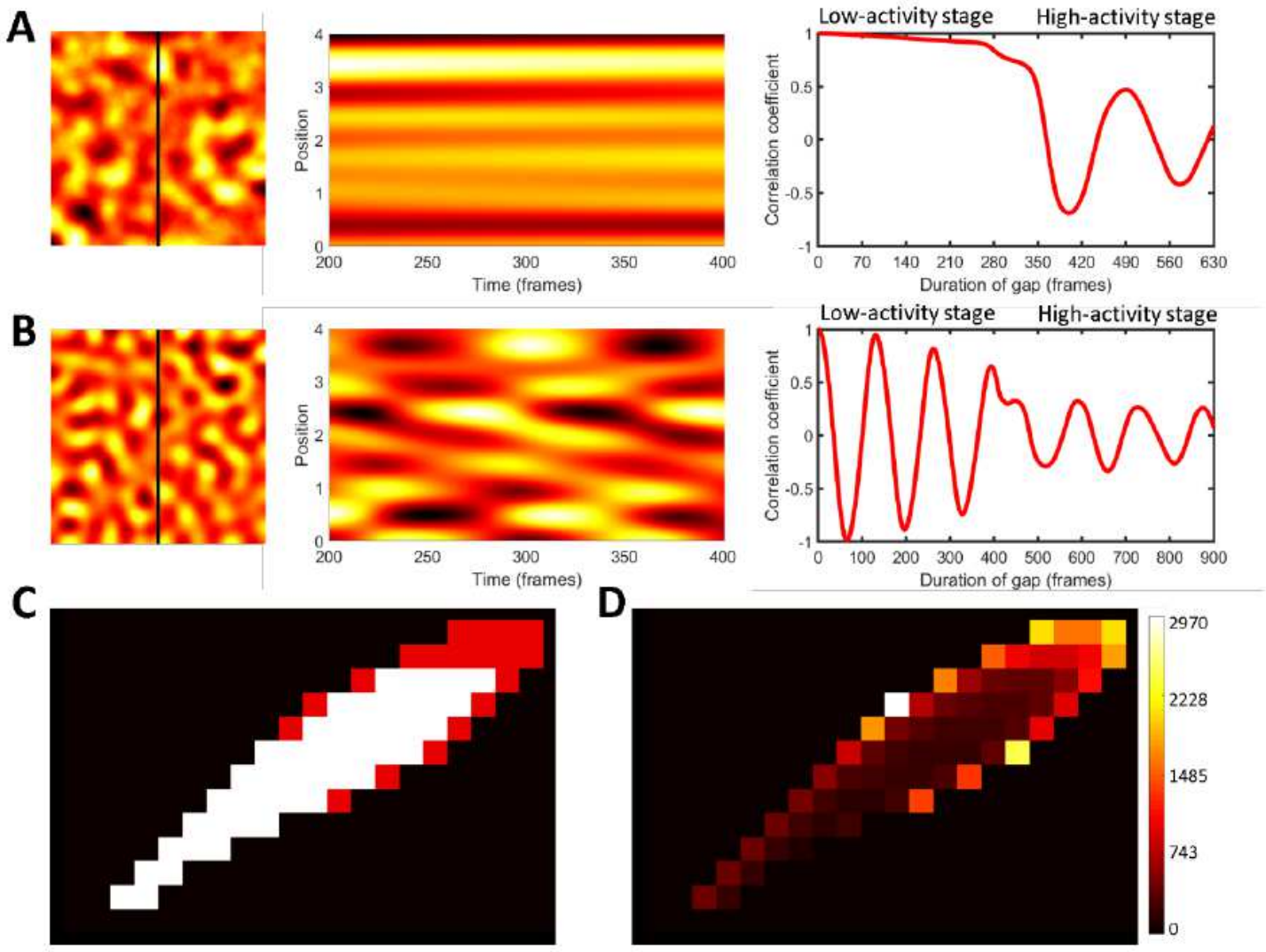

Figure 5

Characteristics of the regimes in the low-activity stage. A, B (Left panels) Snapshots of the system in the quasi-static (□□0=0.2, □□2=0.8) and oscillatory (□□0=0.2, □□2=1.1) regimes of the low-activity stage; top and bottom panels respectively. (Central panels) Kymograph of the system dynamics along a line shown in black in the left panels. (Right panels) Temporal autocorrelation plots, showing the correlation coefficient as a function of the time lag (see Methods). C. Classification of the parameter space with white and red colors indicating the quasi-static and oscillatory regimes, respectively. D. Colormap showing the duration of the low-activity stage (in simulation time).

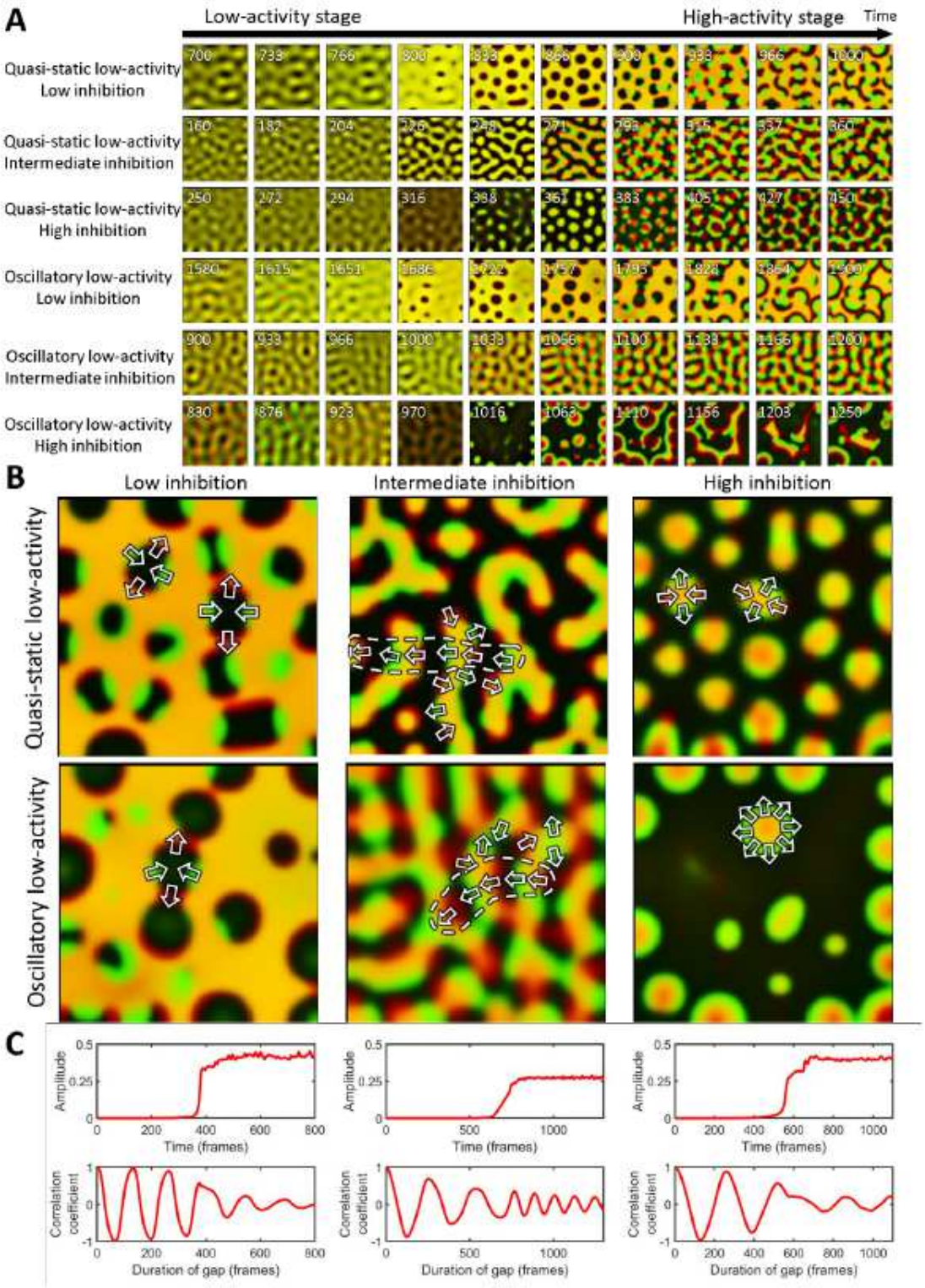

Figure 6

The transition of the system between the low- and high-activity stages. A. Snapshots of the patterns at low- and high- activity stages for different values of the inhibition strength: (1) weak (□□0=0.18, □□2=0.7 for quasi-static and □□0=0.2, □□2=0.75 for oscillatory regimes), (2) balanced (□□0=0.2, □□2=0.9 for quasi-static and □□0=0.26, □□2=1.05 for oscillatory regimes), and (3) strong (□□0=0.22, □□2=1.1 for quasi-static and □□0=0.2, □□2=1.1 for oscillatory regimes). B. Snapshots of the system at the beginning of the high-

activity stage. Arrows indicate the direction of wave propagation. Dashed outlines indicate vector alignment on a larger scale. Images in A, B show two merged channels: green for the activator and red for the inhibitor. C. The activity amplitude and temporal autocorrelation for the oscillatory low-activity stage with weak negative feedback (left), balanced activation and inhibition (center), and strong negative feedback (right).

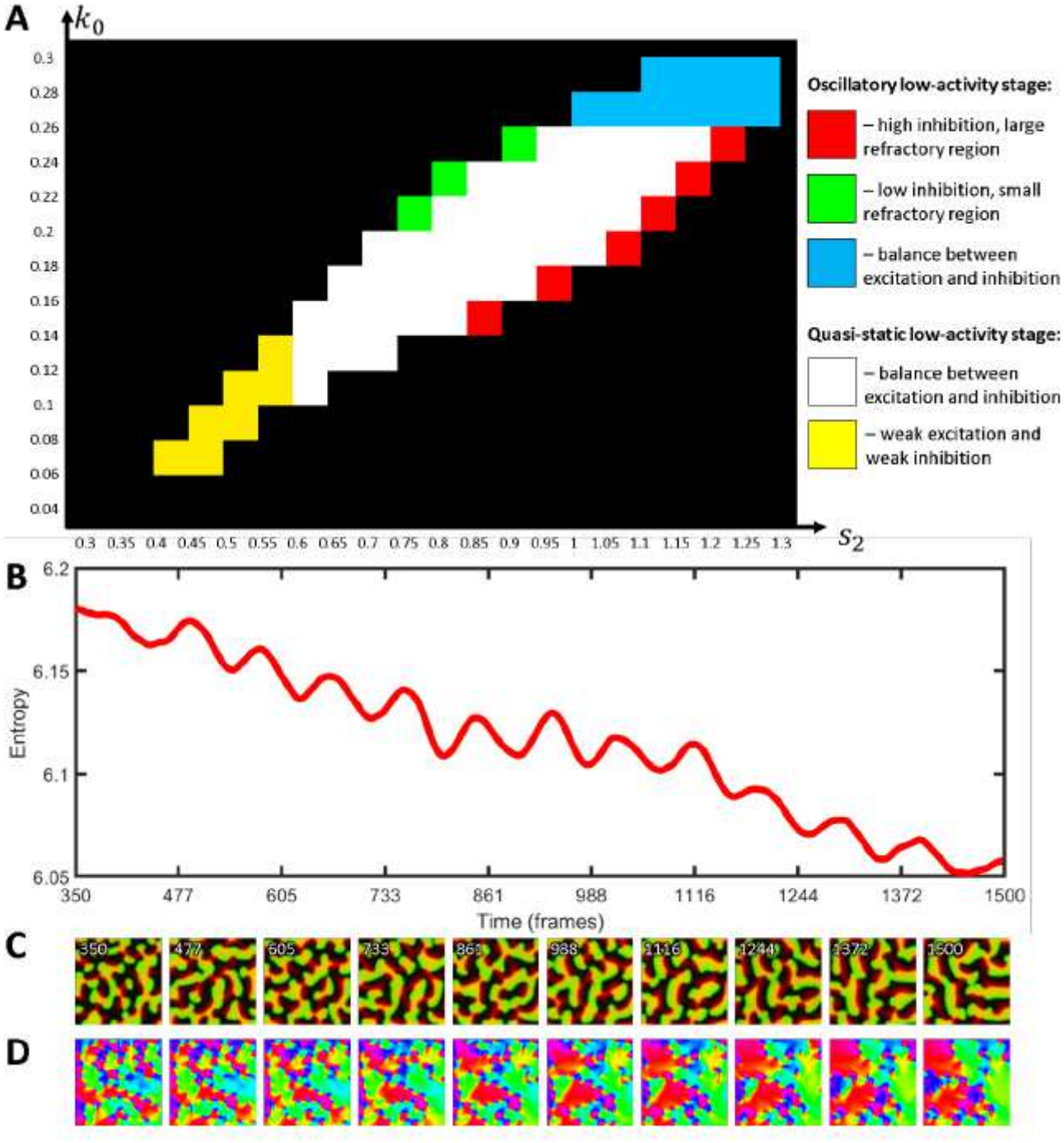

Figure 7

Classification and long-term dynamics of wave domains. A. Different types of system's behaviors in the space of parameters representing the basal activation rate and the strength of negative feedback. B. Textural entropy as a function of time during the growth of wave domains (□□0=0.15, □□2=0.8). C.

Snapshots from the simulation in B with the simultaneous visualization of the inhibitor and activator in the system (merged channels). D. Colormaps of the direction of wave propagation in C showing the increasing size and decreasing number of the wave domains over time. The values of wave vector angles were averaged with a running window of 100 time steps of the simulation

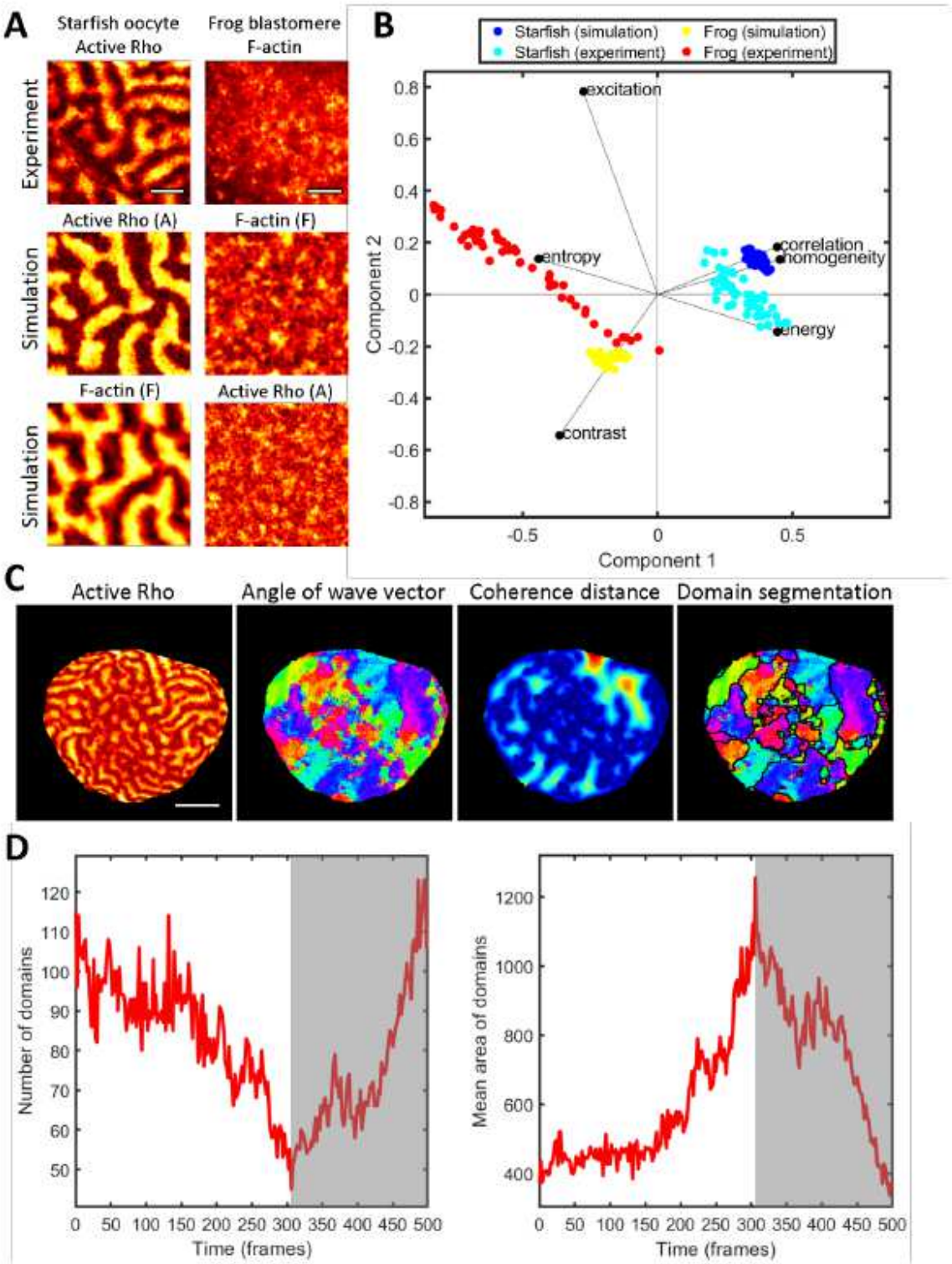

Figure 8

Quantitative analysis of active Rho and F-actin patterns in experimental data and simulation. A. An example of starfish (active Rho) and frog (F-actin) cortical dynamics with the corresponding simulation results representing both active Rho and F-actin signals. The scale bar is 20 μm. B. Biplot representing the results of PCA analysis of simulation and experimental data. Active Rho signal was used for starfish data and F-actin for frog data. 50 consecutive frames were used from each dataset for the analysis. C. The pipeline of wave domain identification in starfish images, including active Rho pattern, colormap of wave vector directions, colormap of the coherence distance, and wave domain segmentation. The scale bar is 50 μm. D. The mean size of wave domains as a function of time for starfish oocyte. The grey area indicates the period of time after the sharp switch in the cell behavior.

Supplementary Files

This is a list of supplementary files associated with this preprint. Click to download.

- SupplementalMaterialsFinal.pdf
- SupplementalVideo1.mp4
- SupplementalVideo2.mp4
- SupplementalVideo3.mp4
- SupplementalVideo4.mp4
- SupplementalVideo5.mp4
- SupplementalVideo6.mp4